Late Cenozoic tephrostratigraphy offshore the southern Central American Volcanic Arc: 1. Tephra ages and provenance

J. C. Schindlbeck[1], S. Kutterolf[1], A. Freundt[1], G. E. Alvarado[2,3], K.-L. Wang[4], S. M. Straub[5], S. R. Hemming[5], M. Frische[1], and J. D. Woodhead[6]

[1]GEOMAR Helmholtz Centre for Ocean Research Kiel, Kiel, Germany, [2]Instituto Costarricense de Electricidad, San José, Costa Rica, [3]Centro de Investigaciones Geológicas, Universidad de Costa Rica, San José, Costa Rica, [4]Institute of Earth Sciences, Academia Sinica, Taipei, Taiwan, [5]Lamont-Doherty Earth Observatory, Columbia University, Palisades, New York, USA, [6]School of Earth Sciences, University of Melbourne, Melbourne, Victoria, Australia

Abstract We studied the tephra inventory of 18 deep-sea drill sites from six DSDP/ODP legs (Legs 84, 138, 170, 202, 205, and 206) and two IODP legs (Legs 334 and 344) offshore the southern Central American Volcanic Arc (CAVA). Eight drill sites are located on the incoming Cocos plate and 10 drill sites on the continental slope of the Caribbean plate. In total, we examined ∼840 ash-bearing horizons and identified ∼650 of these as primary ash beds of which 430 originated from the CAVA. Correlations of ash beds were established between marine cores and with terrestrial tephra deposits, using major and trace element glass compositions with respect to relative stratigraphic order. As a prerequisite for marine-terrestrial correlations, we present a new geochemical data set for significant Neogene and Quaternary Costa Rican tephras. Moreover, new Ar/Ar ages for marine tephras have been determined and marine ash beds are also dated using the pelagic sedimentation rates. The resulting correlations and provenance analyses build a tephrochronostratigraphic framework for Costa Rica and Nicaragua that covers the last <15 Myr. We define 39 correlations of marine ash beds to specific tephra formations in Costa Rica and Nicaragua; from the 4.15 Ma Lower Sandillal Ignimbrite to the 3.5 ka Rincón de la Vieja Tephra from Costa Rica, as well as another 32 widely distributed tephra layers for which their specific region of origin along Costa Rica and Nicaragua can be constrained.

1. Introduction

Plinian and ignimbrite eruptions producing widely dispersed ash clouds are an integral part of arc volcanism, particularly in ocean-continent subduction zones. The widespread ash layers are best preserved in mostly nonerosive marine and lacustrine environments, which thus provide the most complete record of such highly explosive volcanic activity over long timescales [*Keller et al.*, 1978; *Ledbetter*, 1985; *Carey*, 2000; *Carey and Sigurdsson*, 2000; *Kutterolf et al.*, 2008a]. Wide aerial distribution across sedimentary facies boundaries, near-instantaneous emplacement, unambiguous chemical compositions, and the presence of minerals suitable for radio-isotopic dating make these ash layers excellent stratigraphic marker beds in marine sediments and provide constraints on the temporal evolution of both the volcanic source region and the ash-containing sediment facies [e.g., *Kutterolf et al.*, 2008a, 2008b, 2008c, 2008d].

Fertile soils, mineral resources, and trading hubs are persistent reasons for high population densities and infrastructure concentrations in subduction zones, which increase vulnerability from volcanic hazards. Understanding the long-term evolution of volcanic systems is one important way of assessing future volcanic hazards [e.g., *Freundt et al.*, 2006; *Kutterolf et al.*, 2013], and tephra layers in marine sediments play a key role in this respect, if they can be linked to their source region [e.g., *Alloway et al.*, 2007; *Kutterolf et al.*, 2008a; *Machida*, 1999; *Ponomareva et al.*, 2013].

In this contribution we focus on (a) tephrostratigraphic correlations between DSDP/ODP/IODP sites in the Pacific Ocean offshore from Costa Rica and (b) the correlation of marine tephras to volcanic deposits on land at the CAVA, to (c) finally establish a chronotephrostratigraphy for highly explosive eruptions spanning the last ∼8 Myr. As a by-product our data constrain the pelagic sedimentation rates in the eastern Pacific between 8°N and 10°N during that period of time. In the companion paper (Part 2) we will discuss the

implications for the Late Cenozoic explosive volcanism in southern Central America and the southern Central American continental margin.

2. Geological Background

The CAVA extends from the Mexico-Guatemala border to central Costa Rica, parallel to the Middle American Trench (MAT; Figure 1), where the Cocos plate subducts beneath the Caribbean plate at a convergence rate of 70–90 mm/a [*Barckhausen et al.*, 2001; *DeMets*, 2001]. Slightly oblique subduction causes tectonic segmentation of the arc [*DeMets*, 2001; *Funk et al.*, 2009] and subduction conditions such as state of hydration of the Cocos plate and composition of its sediment cover, slap dip angle, and upper plate crustal thickness and composition vary significantly along the subduction zone [*Abers et al.*, 2003; *Plank et al.*, 2002; *Hoernle et al.*, 2002; *Syracuse and Abers*, 2006; *Carr*, 1984]. Moreover, the Cocos Ridge, the track of the Galápagos hot spot, subducts beneath Costa Rica [*Hoernle et al.*, 2000; *Gazel et al.*, 2009] and its geochemical signature is carried northward by arc-parallel mantle flow [*Hoernle et al.*, 2008]. All these influences cause systematic variations in geochemical compositions of Quaternary volcanic rocks along the arc, and between arc segments, which have been extensively studied [*Carr*, 1984; *Carr et al.*, 1990, 2003, 2007a; *Feigenson and Carr*, 1986; *Feigenson et al.*, 2004; *Hoernle et al.*, 2008; *Patino et al.*, 1997, 2000; *Freundt et al.*, 2014]. Of particular interest here are the four segments of the southern CAVA, which also differ in the geochemical compositions of their magmatic rocks [*Hoernle et al.*, 2008; *Bolge et al.*, 2009]. Quaternary volcanic rocks of Costa Rica are calc-alkaline, accompanied by some island arc tholeiites and some rare alkaline volcanic rocks from the back arc [*Alvarado and Carr*, 1993; *Tournon and Alvarado*, 1997]. The primary compositional differences, complemented by temporally and regionally varying degrees of magmatic differentiation from basalts through rhyolites, are useful for marine-terrestrial stratigraphic correlations in the Late Pleistocene and Holocene [*Kutterolf et al.*, 2008a], especially in the Nicaraguan segments [*Kutterolf et al.*, 2007a, 2007b].

However, this geochemical approach can also be applied to the less well known Neogene CAVA. Slab roll-back at Nicaragua has shifted the volcanic front westward so that the Neogene arc remains exposed. These lavas have been dated by *Ehrenborg* [1996], *Plank et al.* [2002], and *Jordan et al.* [2006, 2007a, 2007b] and show that regional geochemical variations, comparable to the Quaternary CAVA, existed during Neogene times. Gaps in volcanic activity during the Miocene to Pleistocene have been reported for Nicaragua [e.g., *Plank et al.*, 2002; *Jordan et al.*, 2007a, 2007b] but appear to become smaller as more age data become available [*Saginor et al.*, 2011a, 2011b].
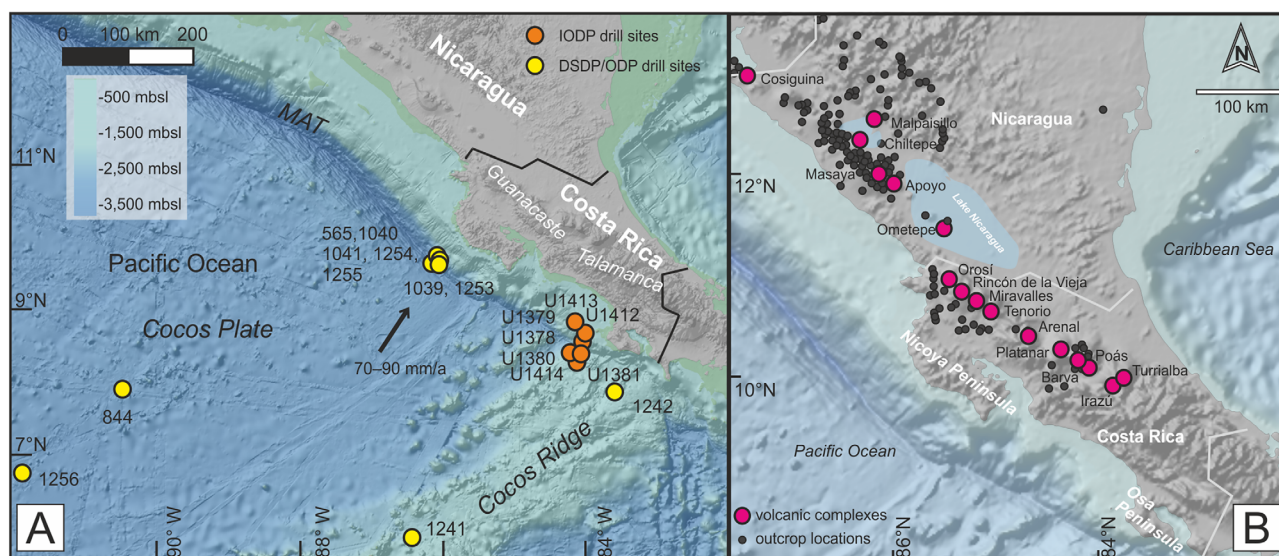
Figure 1. (A) Overview map of Central America. Map created using GeoMapApp (http://www.geomapapp.org; GMRT-Global Multi-Resolution Topography) [*Ryan et al.*, 2009]. Yellow/orange circles indicate drill site positions of deep-sea drilling programs. The black arrow indicates the direction of the Cocos Plate motion and relative velocity to the Caribbean Plate after *DeMets* [2001]. (B) Close-up showing Holocene eruption centers in southern Nicaragua and Costa Rica (magenta circles) and sample locations of comparative tephras.

In Costa Rica, subduction-related volcanism has occurred at least since the Upper Cretaceous, but more extensive volcanism developed between the Oligocene and Quaternary. *Plank et al*. [2002] studied geochemical characteristics indicative of long-term changes in sediment subduction and *Gazel et al*. [2009] investigated the geochemical influence of subduction of the Galápagos hot spot track on Neogene volcanism in Costa Rica and Panama.

2.1. On-Shore Tephrostratigraphy

As a prerequisite to understand the correlations with the marine tephra beds to be made in later sections, we briefly summarize the tephra record known from land in Figure 2. A number of publications have investigated the Late Pleistocene to Holocene tephrostratigraphic successions in Costa Rica and Nicaragua and the stratigraphic succession of major tephras spanning the last ~70 ka is fairly well known [*McBirney and Williams*, 1965; *Bice*, 1985; *Freundt et al*., 2006, 2010; *Kutterolf et al*., 2008a, 2008b, 2008c, 2011; *Pérez et al*., 2006; *Pérez and Freundt*, 2006; *Scott et al*., 2006; *Self et al*., 1989; *Stoppa*, 2015; *Wehrmann et al*., 2006; *Vogel et al*., 2004, 2007; *Alvarado and Gans*, 2012; *Alvarado et al*., 1992; *Chiesa*, 1991; *Chiesa et al*., 1992; *Deering et al*., 2007; *Gillot et al*., 1994; *Zamora et al*., 2004]. During this late Pleistocene to recent period, very large magnitude caldera eruptions only occurred in El Salvador and Guatemala [e.g., *Weyl*, 1980; *Rose et al*., 1999] but some of their distal ashes reached the southern CAVA [*Kutterolf et al*., 2008a].

Knowledge of older volcaniclastic formations is rudimentary at best. Figure 2 indicates older formations (gray boxes) at many of the volcanic complexes from Cosigüina to Barva and Irazú as reported in *Longpré et al*. [2014], *Stoppa* [2015], *Kutterolf et al*. [2007a, 2011], *Pérez et al*. [2009], *Sussman* [1985], *Wehrmann et al*. [2006], *Girard and Van Wyk de Vries* [2005], *Borgia and Van Wyk de Vries* [2003], *Martinez and Viramonte* [1971], and *Alvarado and Gans* [2012].

The temporal extent of these older formations is typically not known or poorly constrained. *Carr et al*. [2007b] proposed volcanism at the modern Nicaraguan arc to be younger than 600–330 ka while published radiometric ages from the Neogene arc in the eastern highlands of Nicaragua range 4.3–25.5 Ma [*Ehrenborg*, 1996; *Jordan et al*., 2006, 2007a, 2007b; *Weyl*, 1980]. Hence, the exact timing of the arc jump remains unclear.

A number of Quaternary widespread, voluminous tephras, mostly ignimbrites, are known from Costa Rica (Figure 2) [*Alvarado and Gans*, 2012]. Prominent are the ~0.6–1.6 Ma Liberia Formation and the ~2 to ~8 Ma Bagaces Formation, both dominantly composed of voluminous silicic ignimbrites that may be related to now mostly hidden older caldera structures (Cañas Dulces and Guayabo calderas) identified by geothermal drilling (Figure 2) [*Vogel et al*., 2004; *Alvarado and Gans*, 2012; *Chiesa*, 1991; *Zamora et al*., 2004; *Szymanski et al*., 2013].

The CAVA terminates at Turrialba, because shallow subduction of the Cocos Ridge prevents volcanism further south [*Alvarado et al*., 1992]. However, volcanism commences in Panama where volcanic activity of the past 2 Ma has mainly produced volcanic rocks of adakitic compositions [e.g., *Defant et al*., 1992]. We do not consider Panama further because we have not found equivalent compositions in our cores.

2.2. Previous Marine Studies

Ash beds were investigated in DSDP/ODP/IODP drill cores and in sediment gravity cores along the CAVA in the Pacific Ocean and the Caribbean Sea [e.g., *Clift et al*., 2005; *Kutterolf et al*., 2007b,a; *Ledbetter*, 1985; *Bowles et al*., 1973; *Jordan et al*., 2006]. The Pacific ash beds form a tephrostratigraphic framework of large CAVA eruptions over the last 200 ka [*Kutterolf et al*., 2007b, 2008a]. *Schindlbeck et al*. [2015] identified Miocene basaltic and rhyolitic tephras emplaced at IODP Site U1381 offshore southern Central America by Plinian eruptions at the Galápagos hot spot. The ODP cores of the Caribbean Sea contain Neogene ash beds from source volcanoes at the Lesser Antilles and in Honduras and Nicaragua [*Jordan et al*., 2007b].

3. Methods

3.1. Sample Locations

3.1.1. Deep-Sea Drilling Cores

We used six DSDP/ODP legs (Legs 84, 138, 170, 202, 205, and 206) and two IODP legs (Legs 334 and 344) with their corresponding eight deep-sea drilling sites on the incoming Cocos plate (Sites 844, 1039, 1241,
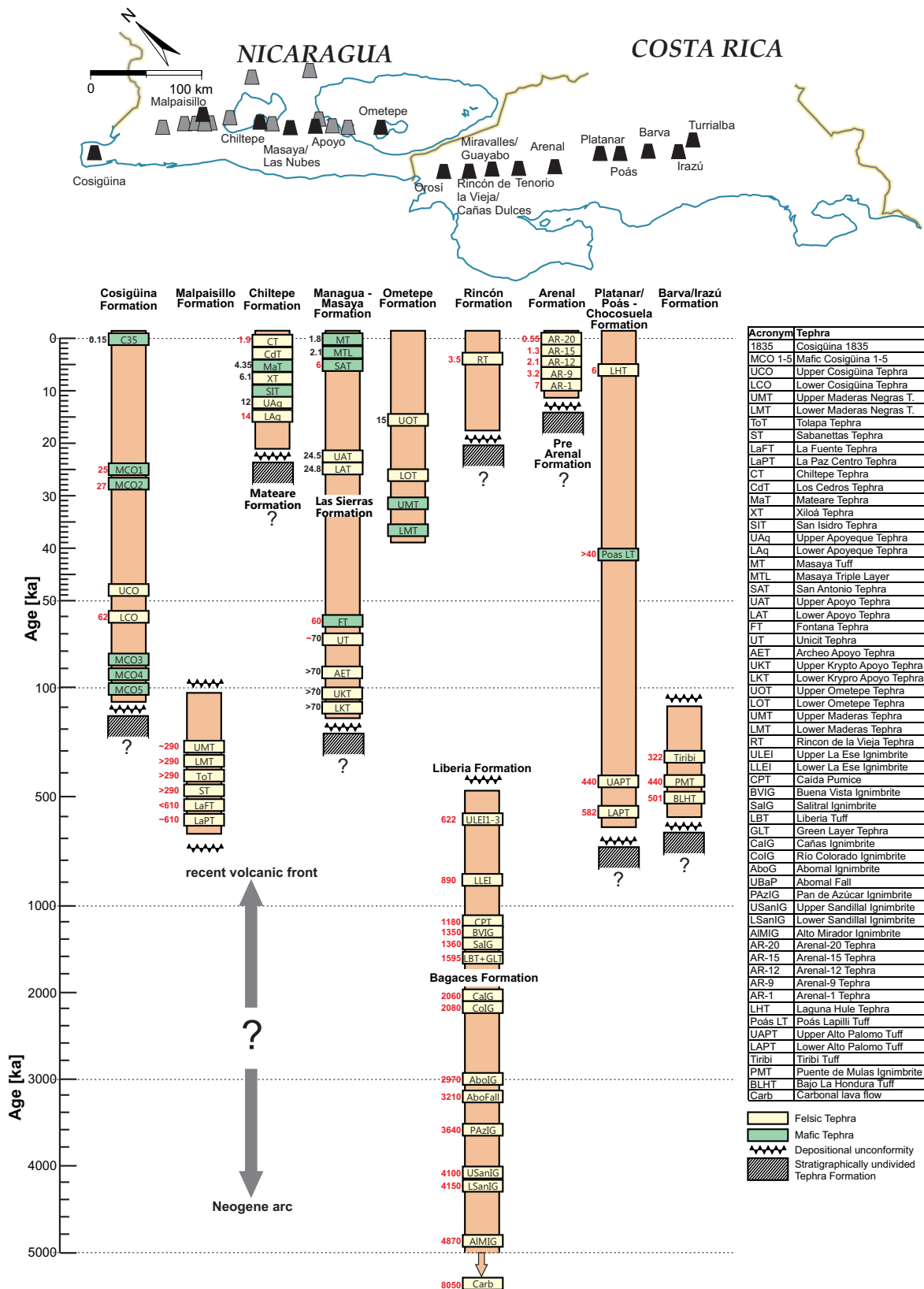
Figure 2. Simplified composite stratigraphic successions of known Pliocene to Holocene major tephras in Costa Rica and Nicaragua [after *Soto and Alvarado*, 2006; *Kutterolf et al.*, 2008a, 2016; *Alvarado and Gans*, 2012; *Stoppa*, 2015; *Prosser and Carr*, 1987]; tephra acronyms are given in the table to the right.

1242, 1253, 1256, U1381, and U1414) and 10 sites (Sites 565, 1040, 1041, 1254, 1255, U1378, U1379, U1380, U1412, U1413) on the continental slope offshore from the southern CAVA, for the systematic investigation of ash beds found in deep marine sediments (Figure 1). Most drill sites form one cluster offshore from the Nicoya Peninsula in northern Costa Rica and another cluster offshore from the Osa Peninsula in southern Costa Rica (Figure 1). During the two IODP expeditions ash beds were sampled shipboard while the other cores were sampled at the IODP Gulf Coast Repository at the Texas A&M University, College Station, TX. In the following we will use the term "ash bed" for a bed or zone in a drill core that is dominantly composed of volcanic ash. We define ash beds that are correlated between sites and/or with tephras on land to form a "tephra layer." With these definitions, a tephra layer represents one volcanic eruption but it can include several ash beds, i.e., occur in several drill locations. As we will show below, we have analyzed 650 primary ash beds and thereby identified 71 tephra layers.

3.1.2. Terrestrial Samples

In order to obtain glass compositions for comparison with the marine samples, we sampled known Middle Pleistocene and the Late Miocene terrestrial fallout layers and ignimbrites from Costa Rica (Figures 2 and 3) [see *Alvarado and Gans*, 2012] as well as fallouts and ignimbrites of that time span in Costa Rica and Nicaragua that lacked detailed published studies. All locations we sampled in 2013 are shown in Figure 1b and coordinates of the localities are provided in Supporting Information Table S1. Supporting Information Table S6 reports the new glass analyses from major Costa Rican tephra deposits that were exclusively used to establish the geochemical correlations. Additionally, we used data published by *Prosser and Carr* [1987], *Hannah et al.* [2002], *Clift et al.* [2005], *Kutterolf et al.* [2008a], *Szymanski et al.* [2013], and *Stoppa* [2015].

3.2. Methods and Analytical Techniques

Marine ash samples were cleaned by disintegration in an ultrasonic bath, if necessary, and subsequently wet-sieved into different grain size fractions (63–125, 125–250, >250 μm and if necessary 32–63 μm). Terrestrial samples were cleaned by disintegration in an ultrasonic bath and altered rims were removed, if necessary. Samples were crushed afterward with a hammer and wet-sieved in the same way as the marine ash samples. The 63–125 μm fraction was further used for compositional analysis of glass shards with an electron microprobe (EMP) and by Laser Ablation Inductively Coupled Plasma-Mass Spectrometry (LA-ICP-MS). All major and trace element data and standard analyses are provided in Supporting Information Tables S2–S6. Phenocrysts of feldspar (sanidine and plagioclase) were separated to carry out $^{39}Ar/^{40}Ar$ age-dating at Lamont-Doherty Earth Observatory (for details see Table 1 and Supporting Information Data Set S8 and S9). Clean glass shards, pumice and scoria particles from the fraction >125 μm were handpicked under the binocular microscope for the analysis of radiogenic isotopes of Pb, Sr, Nd, and Hf (MC-ICP-MS). Isotope analyses were performed at Lamont-Doherty Earth Observatory/U.S.A. and at Melbourne University/Australia. A detailed method section is provided in Supporting Information Data Set S1 [*Cai et al.*, 2014; *Maas et al.*, 2005; *Münker et al.*, 2001; *Nowell et al.*, 1998; *Pin et al.*, 1994; *Pin and Santos-Zalduegui*, 1997; *Todt et al.*, 1996; *Woodhead and Hergt*, 2001] and the data are reported in Table S7.

3.2.1. EMP

Glass shard analyses (~16,000 in total) for major and minor elements were conducted on epoxy embedded samples using a JEOL JXA 8200 wavelength dispersive EMP at GEOMAR, Kiel adopting the methods from *Kutterolf et al.* [2011]. Accuracy was monitored by standard measurements on Lipari obsidian (rhyolite) [*Hunt and Hill*, 2001] and Smithsonian basaltic standard VGA. Sixty individual glass shard measurements are bracketed by four standard measurements (two measurements per standard). Standard deviations of measured elements are <0.5% for major, and <10% for minor elements (with the exception of P_2O_5 and MnO_2 in samples >65 wt % SiO_2). All analyses are normalized to 100% to eliminate the effects of variable postdepositional hydration and minor deviations in the electron beam focus. Analyses with total oxides less than 90 wt % were excluded from the data set to avoid the effects of alteration throughout all elements. Some ~13,000 microprobe analyses passed the quality check, which also excluded accidental shots on microcrystals. The remaining analyses for each sample were then averaged in order to characterize the elemental compositions of each individual tephra.

3.2.2. LA-ICPMS

Trace and selected major element concentrations of ~750 glass shards were measured by LA-ICP-MS mainly at two laboratories in Taipei, Taiwan (between 2013 and 2016), as well as at GEOMAR Helmholtz Center for Ocean Research Kiel (Germany) in April 2011.
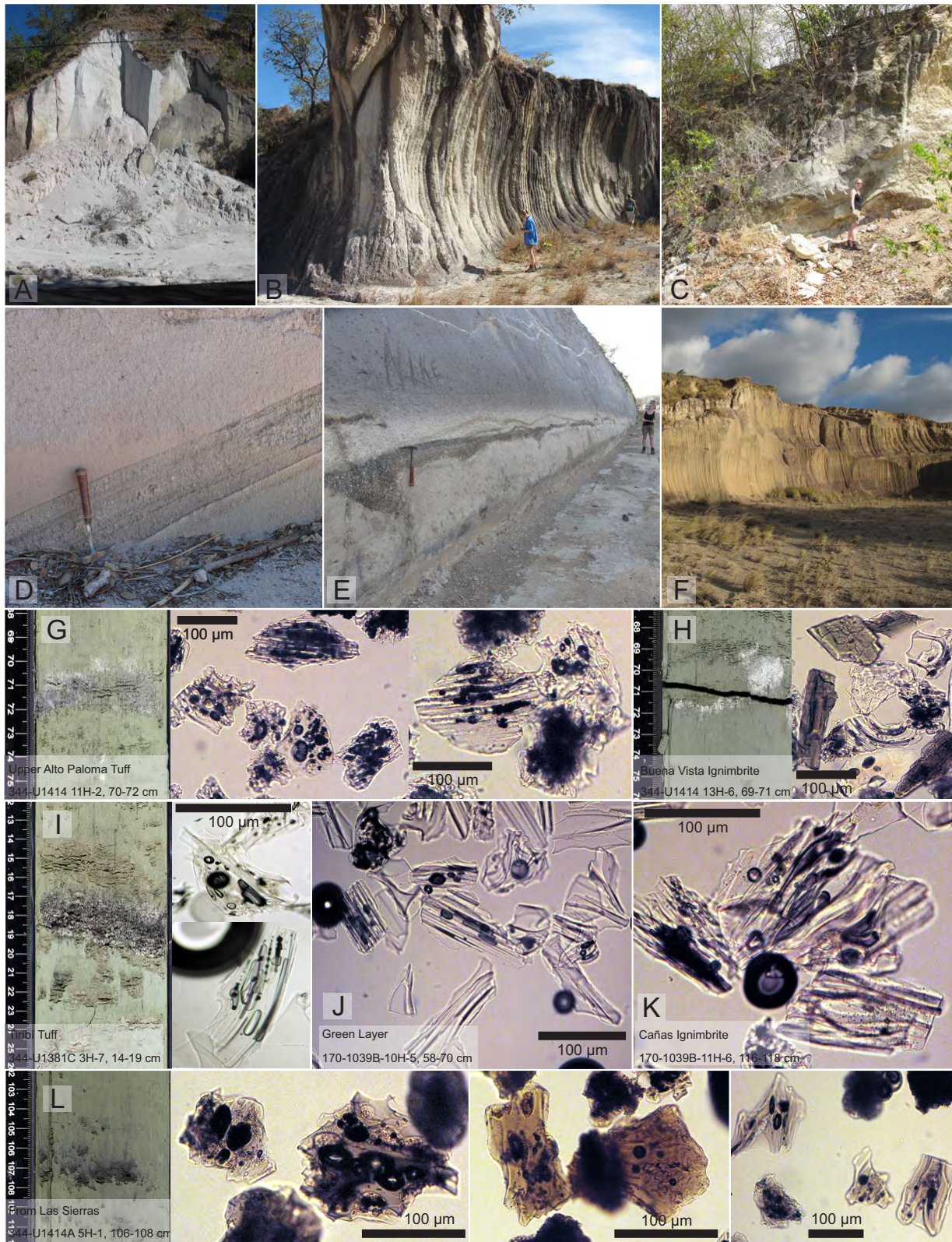
Figure 3. Selected outcrop photographs of major sampled tephras on land. A = Liberia Tuff, B = Buena Vista Ignimbrite, C = Lower Sandillal Ignimbrite, D = Green Layer, E = Meco Plantel Ignimbrite (Bagaces Formation), F = La Ese Ignimbrites. See Figure 2 for stratigraphic information. (G–L) Core photographs of selected marine ash beds and smear-slide microphotographs of their vitric ash particles. Labels give position in core and name of the correlative tephra on land.

Table 1. Ages for ODP/IODP Ash Beds Offshore Southern CAVA Obtained by Ar/Ar Dating (For Details See Supporting Information Data Set S8 and S9)

Interval	Lab ID	Mineral	Age (Ma)	±Error (Ma)/(%)	MSWD	Reference
170-U1039B-10H-5, 58–70 cm	16665	Plagioclase	1.81	0.11 (6.0)	2.32	This study
170-U1039B-36X-4, 147–150 cm	16802	Sanidine	15.24	0.03 (0.18)	7.76	This study
202-1241B-25H-7, 12–18 cm	16801	Sanidine	8.15	0.16 (2.0)	0.42	This study
344-U14141A-38R-1, 76–78 cm	16797	Plag	12.05	0.11 (0.91)	16.03	This study
344-U1381C-9H-2, 41–43 cm	16495	Plag	12.0	1.2 (6.7)	0.65	*Schindlbeck et al.* [2015]
344-U1381C-10H-2, 96–98 cm	16494	Sanidine	13.92	0.03 (0.2)	0.24	*Schindlbeck et al.* [2015]

The LA-ICP-MS analyses at GEOMAR were made using a double-focusing, magnetic sector mass spectrometer (Nu-Instruments, AttoM), which is coupled to a 193 nm Excimer laser ablation system (Coherent, GeoLasPro). Ablation was performed in a pure Helium atmosphere. Additionally, argon carrier gas was mixed to the sample aerosol prior to the plasma torch. Spot analyses were performed by 100 s ablation at a laser repetition rate of 3 Hz, using a spot diameter of 16 μm and a fluence of 8 J/cm^2. A 50 s gas background was collected prior to each ablation. Gas flows, torch position, and ion-optics-focusing were optimized in order to provide a maximum in ion transmission, low oxide production rates (ThO/Th ≤0.3%), and fast sample wash-out. The standard NIST SRM610 glass [*Wise and Watters*, 2012] was used for mass calibration. Data were reduced by applying the linear regression slope method [*Fietzke et al.*, 2008]. Silicon was used for internal standardization utilizing data from EMP analyses [see *Kutterolf et al.*, 2014, Supporting Information Table S4].

The detailed machine setups, procedures, and methods of the laboratories at the National Taiwan University are described in *Schindlbeck et al.* [2015] and are complemented here by the description of the analytical procedures utilized during the measurements at the Academia Sinica [*Schindlbeck et al.*, 2016a]. The setup at the Academia Sinica in Taipei, Taiwan, comprises a laser beam (193 nm excimer laser) set to a spot size of 16–30 μm using 5–10 J/cm^2 energy density at 1–5 Hz repetition rate which was coupled to high-resolution ICPMS instruments. Following 45 s of blank acquisition, typical ablation times were around 75 s. Data reduction was performed using Version 4.0 of "real-time online" GLITTER© software [*van Achterberg et al.*, 2001] immediately following each ablation analysis. Silica and calcium concentrations, measured by EMP, were used as internal standards to calibrate the trace element analyses. International standard glass (BCR-2G) was measured every five to eight samples to monitor accuracy and to correct for matrix effects and signal drift in the ICP-MS, as well as for differences in the ablation efficiency between the sample and the reference material [*Günther et al.*, 1999]. Elemental concentrations in NIST SRM 612, used for external calibration, were taken from *Norman et al.* [1996]. The limit of detection (LOD) for most trace elements is generally no higher than 100 ppb. For REEs, the LOD is generally around 10 ppb. The analytical precision is better than 10% for most trace elements. Repeated measurements of the same samples in different laboratories revealed good replication of the trace elements.

3.2.3. Ar-Ar Dating

Feldspars were leached for 5 min in a 5% HF solution in an ultrasonic bath, rinsed three times with deionized water, and then covered in methanol to remove any adhering glass. Together with Fish Canyon (28.201 ± 0.046 Ma) [*Kuiper et al.*, 2008] sanidines, the samples were coirradiated for 8 h at the USGS TRIGA reactor in Denver. Subsequently, irradiated samples were measured on single-step fusions of single crystals using a CO$_2$ laser to degas the samples, as single steps for the single crystals. Before they entered the mass spectrometer, the gasses were cleaned up by exposure to SAES GP50 getters run at 2 amps. Isotopes were measured in static, peak-hopping mode with an analog multiplier on a VG5400 noble gas mass spectrometer at Lamont-Doherty Earth Observatory/U.S.A. With this setup the conversion is 3.98e13 nannoamps/mole. Measured isotope data were corrected for background contributions based on frequent measurements of the blanks (every three to four samples), mass discrimination based on average measurements of air aliquots through the duration of the sample disk run (every 12 samples), and nuclear interferences based on values characteristic of this reactor (values taken from *Dalrymple et al.* [1981]). Detailed information is provided in *Schindlbeck et al.* [2015] as well as in Supporting Information Data Set S8 and S9.

4. Results and Discussion

4.1. Tephra Inventory

The variably thick intervals of greenish-gray hemipelagic to brownish-grayish-white pelagic sediment at the investigated sites [*Pisias et al.*, 1995; *Kimura et al.*, 1997; *Morris et al.*, 2003; *Mix et al.*, 2003; *Vannucchi et al.*, 2012;
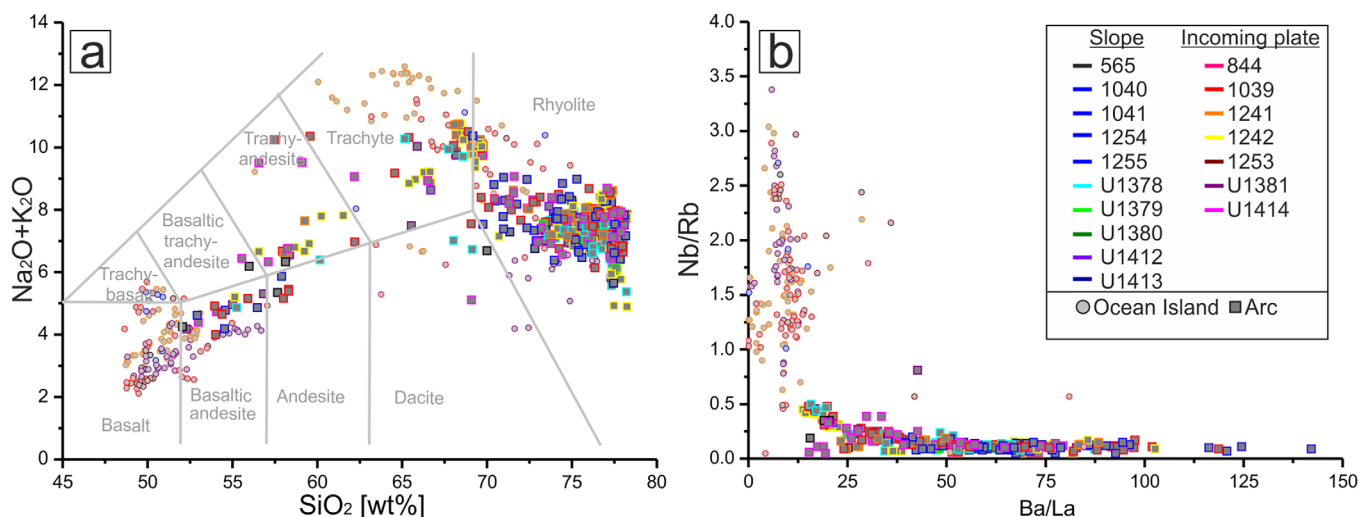
Figure 4. Matrix-glass compositional ranges of marine ash beds (normalized to anhydrous compositions and each symbol is the mean composition per sample). (a) Total alkali versus silica diagram to indicate compositional variability of marine tephras in southern CAVA drill sites (color-coded) across the discrimination grid following *Le Maitre et al.* [2002]. (b) Nb/Rb versus Ba/La discrimination diagram to distinguish tephras with ocean island geochemistry (e.g., Galápagos; circles) from those with subduction-zone (CAVA) geochemistry (squares).

Harris et al., 2013] are intercalated with distinct ash beds ranging from 1 to 60 cm in thickness, horizons of ash pods, and zones of ash dispersed in the marine sediments.

Our sampling and analysis strategy prioritized intact ash beds over pod horizons over ash beds disturbed by erosion or bioturbation. Dispersed ash directly above an ash bed is interpreted as being reworked from this layer, which has been confirmed by geochemical analyses of samples taken in these intervals. Ash-bearing horizons are commonly light gray, pinkish, yellowish to dark gray and black (Figures 3G–I and 3L). Boundaries to the hemipelagic and pelagic background sediments are often sharp at the base and diffuse at the top, sometimes modified by bioturbation. Average grain sizes range from 32 to 500 μm, and the ash beds are overall well to very well sorted. The ash beds are typically massive but often show normal grading.

Glass shards derived from the more evolved ash beds are transparent; the texture is fibrous, blocky, and cuspate (Figures 3G–3I). Pumiceous fragments with elongated, tubular and minor round bubbles also occur. In contrast glass shards from less evolved compositions are (light-)brown and red-brown and mostly have blocky and sometimes fibrous shapes with few round and elongated (tubular) vesicles (Figure 3L). Some glass shards are also tachylitic. The ash beds range from mineral poor (1–5 vol %) to mineral rich (up to 50 vol %); crystal-rich zones particularly occur at the base of coarse ash beds indicating normal density grading. In the order of abundance, feldspar > amphibole and pyroxene ≫ biotite can be observed within the felsic layers, and feldspar ≫ pyroxene ≫ olivine in the mafic ash beds.

Pleistocene and Pliocene ash beds at all sites are dominantly felsic in composition (~80%) (Figure 4a), whereas the distribution of mafic and felsic ash beds in the Miocene units is more equal. Miocene mafic ash beds are dominant (>70%) in Sites U1381, 1241, and 1039 (Figure 4a). We analyzed the compositions of ~840 samples and identified ~650 of these as primary ash beds characterized by homogeneous to zoned glass compositions, in contrast to ash beds with mixed, genetically unrelated glass compositions, which we interpret as reworked deposits. Glass compositions from the primary ash beds in Figure 4a show nearly bimodal distribution of basalt or rhyolite compositions in the subalkalic field, and of trachybasaltic or trachytic compositions in the alkalic field, respectively. Trace element compositions divide the tephra inventory into a subset with ocean-island geochemical signatures (e.g., high Nb/Rb at low Ba/La; Figure 4b) and a subset with arc-volcanic characteristics (e.g., high Ba/La at low Nb/Rb; Figure 4b). The ocean-island subset includes the Miocene ash beds of Site U1381, which *Schindlbeck et al.* [2015] showed originated from Plinian eruptions at the Galápagos hot spot. The majority of the Miocene ash beds of Sites 844, 1039, 1040, 1241, and 1253 share the typical compositions from Site U1381 (Figure 4b), and most likely also derive from the Galápagos region. Additionally, there are Pleistocene ash beds in Site 1241 that show an alkali-rich ocean-island signature and which derive from Cocos Island as discussed in *Schindlbeck et al.* [2016a]. In this contribution, we focus on the stratigraphy and provenance of the remaining 430 ash beds, which have glass

compositions compatible with an origin mainly from Costa Rica, Nicaragua and a small subset from Guatemala and El Salvador (data are provided in Supporting Information Tables S2–S7). We have found no evidence for marine tephras from Panama volcanoes; however, the availability of data on large eruptions from Panama is very limited.

4.2. Tephra Ages

We used direct and indirect dating methods to establish our marine tephrostratigraphic age models. Direct ages of marine tephras are obtained by ^{40}Ar/^{39}Ar dating of feldspar crystals from the ash beds, and by correlation with well-dated tephras on land. We complemented published age data for major tephras on land by four ^{40}Ar/^{39}Ar feldspar ages between 1.81 and 15.24 Ma for marine ash beds from the drill cores; the results are reported in Table 1. As we will show below, 39 marine tephra layers can be unambiguously geochemically correlated to specific deposits of known age on land.

Indirect age data for the marine tephras initially came from the age-depth models derived from magneto- and bio-stratigraphy from the sites [*Kimura et al.*, 1997; *Harris et al.*, 2013; *Mix et al.*, 2003; *Pisias et al.*, 1995].

Using all these age constraints and the timelines provided by directly dated tephras, we converted the intercalated thicknesses of marine sediment to age-depending (hemi-)pelagic sedimentation rates as will be further discussed in Part 2 [*Schindlbeck et al.*, 2016b]. These sedimentation rates allow us to calculate the ages of single ash beds and tephra layers that were not captured by the dating approaches above. The sedimentation rates between two age anchors are average values since we apply linear interpolation. Due to uncertainties in determination of sedimentation rates, these tephra ages have uncertainties ranging up to 14% of their age [cf. *Kutterolf et al.*, 2013]. These ages from sedimentation rates then can provide additional support for cases where the geochemical correlation may be somewhat ambiguous.

Compaction and drilling disturbances, especially in the deeper parts of each hole, may cause differences for age determinations in different sites and holes due to over/underestimated sedimentation rates. We have not accounted for the thickness of the ash layers, which may cause overestimation of the true sedimentation rate due to their instantaneous emplacement. Another source of minor error is the fact that marine sediment is mixed to variable extent with volcanic ash particles. Here we agree with other contributions to the deep-sea drilling program in ignoring corrections for both features, because the cumulative thickness of the ash beds accounts for negligible ~0.3–3.6% of total thickness [see *Schindlbeck et al.*, 2015]. Age deviations of e.g., <10 ka for the last 1.5 Ma at Site U1414 (0.6% discrete ash) or <13 ka for the last 2 Ma at Site 1039 (1.6% discrete ash) are below the accuracy of the Ar/Ar age dating used for the correlated dated terrestrial tephras.

Overall, we observe sedimentation rates of 5–200 m/Ma on the incoming plate and 3–950 m/Ma on the continental slope offshore from the southern CAVA, but the apparent sedimentation rates can vary with depth at both deep marine environments. For sites on the Cocos plate the newly determined sedimentation rates agree well with the sedimentation rates obtained onboard the expeditions but substantial differences can be seen for the sites on the continental slope. The sedimentation rates will be discussed in detail in Part 2.

4.3. Stratigraphy and Provenance

With the exception of Sites U1414, U1378, and U1380 two or more holes were drilled close to each other (~20 m) at each site and core profiles are expected to match closely. This is especially true for Sites 1241 and 1242, where three and four holes were drilled, respectively, and most ash beds can indeed be found in all individual holes.

For correlations we used major and trace element concentrations/ratios of glass shards of the ash beds as well as their relative stratigraphic position. Correlations were made adopting the methods described in *Kutterolf et al.* [2008a]. We emphasize that correlations are constrained not only by one element/ratio but also by multiple geochemical overlaps of major and (if available) trace elements, and are further supported by tephra ages. Generally, the number of correlations between the holes depends on the number of ash beds recovered in the cores, and recovery depends on drilling conditions and methods. For example, at Site U1381 hole A was drilled with the RCB (Rotary Core Barrel) method while APC (Advanced Piston Coring) was used for hole C, providing much better preservation and recovery of the drilled sediments [e.g., *Huey et al.*, 2009].

However, we were still able to correlate 353 ash beds between two or more sites, 26 correlations connect ash beds between three or more sites, and we found correlations between all sites along >250 km of the MAT providing major tie points for a regional tephrostratigraphy covering the 0.2 to ∼6.5 Ma age range. Most correlations were found between Site 1039, offshore Nicoya Peninsula (North-Costa Rica) and Site U1414, offshore Osa Peninsula (South-Costa Rica).

Correlations of marine ash beds to their terrestrial equivalents and respective source volcanoes are mainly based on glass chemical compositions as the most distinctive characteristic but modal, lithological, stratigraphic, and textural observations were also considered. Figures 5 and 6 show examples of chemical variation diagrams that turned out to be most useful for the purpose of chemical fingerprinting. Colored correlation fields for tephras on land are based on the new glass data and complemented by published data (for further variation diagrams see Supporting Information Figures S1 and S2).

We have established 39 marker tephra layers, called tephra layers *A* to *T* with subdividing numbers, that correlate between the different drill sites (comprising 226 individual ash beds) and with volcanoes or specific tephras or tephra formations on land in Costa Rica and Nicaragua (Table 2 and Figures (5 and 6), S1, and S2). The alphabetic order is also the order of increasing age; tephra layer *A* correlates with the 3.5 ka Rincón de la Vieja Tephra (RT) from Costa Rica and tephra *T* with the 4.15 Ma Lower Sandillal Ignimbrite (LSanIG; Figure 2) from Costa Rica.

Of the remaining 204 felsic and mafic ash beds, 127 can be correlated between sites and form the 32 tephra layers called *s1–s32* (Figures 7 and S3 and Table 3). The remaining 77 individual ash beds are numbered within their respective site (see Supporting Information Data Set S2 and S3). However, none of these ash beds or tephra layers could be correlated to a specific tephra deposit on land. In order to at least identify the potential region of their origin at the arc, we compared the trace element and isotope characteristics with the geochemical variations from Costa Rica and Nicaragua on land, thereby considering the age relationships of the marine ash beds or tephra layers with respect to temporal changes in the along-arc variations. Along-arc geochemical variations, particularly in trace element ratios and radiogenic isotope characteristics (e.g., in La/Sm, Pb/Nd, Ba/Nb, Ba/Th, Ba/La, U/Th, and ^{207}Pb/^{204}Pb and ^{143}Nd/^{144}Nd; Figures (7 and 8), and S3), have been extensively documented for the Quaternary volcanic front [*Carr et al.*, 2003, 2007a; *Carr*, 1984; *Feigenson and Carr*, 1986; *Patino et al.*, 1997, 2000; *Hoernle et al.*, 2002; *Feigenson et al.*, 2004; *Kutterolf et al.*, 2008a,]. Less abundant data are available for the Neogene arc rocks [*Plank et al.*, 2002; *Jordan et al.*, 2007b; *Carr et al.*, 2007a; *Vogel et al.*, 2004] and we have complemented that data set with our new Neogene samples and analyses (see Supporting Information Table S6). The Neogene Coyol arc (Nicaragua and Honduras) has predominantly silicic volcanic products [e.g., *Ehrenborg*, 1996], with high La/Sm, Rb/Nd, Rb/Hf, ^{208}Pb/^{204}Pb, and low Ba/La, Ba/Th, Nb/Ta, ^{143}Nd/^{144}Nd ratios probably reflecting some influence of continental crust on magma genesis [e.g., *Jordan et al.*, 2007a] (Figures 7 and 8, and S3).

In the along-arc diagrams we distinguished between the Quaternary and the Neogene arc but both show systematic changes of trace element and isotope characteristics along Costa Rica and Nicaragua that make it possible to allocate the region of origin of the investigated marine tephra layers. In Figures (7 and 8), and S3 ellipsoids represent the specific compositional ranges of the tephra layers (*s1–s32*; Figures 7 and S3) and individual marine ash beds (Figure 8), which we have projected onto the respective along-arc compositional fields of Costa Rica and Nicaragua. Regions along the arc that show the same overlapping compositional range over multiple elemental ratios qualify as potential source regions for the tephras. In Figures (7 and 8), and S3 we have chosen trace element and isotope ratios that best identify the major source regions of our samples in Costa Rica and Nicaragua but we have checked the implied regional correlations against other geochemical parameters as well. Although correlations to northern CAVA sources are possible, we concentrate on the correlations to Costa Rica and Nicaragua sources, considering the proximity of the drill sites. The northern CAVA marine tephra inventory and provenance in DSDP/ODP sites offshore Guatemala will be presented elsewhere.

In the following we describe all correlations between individual marine ash beds or tephra layers and terrestrial tephra deposits or possible volcanic sources in geographic order of the source volcanoes from south to north along the CAVA in order to elucidate the new implications of the marine tephra record (Figure 9) for the history of the volcanic systems.

Figure 5. K_2O versus SiO_2 variation diagrams of marine ash beds (*A* to *T*) compared with glass-composition fields of known Holocene to Pliocene tephras on land (normalized to anhydrous compositions). Our data for terrestrial eruptions is complemented by data from *Prosser and Carr* [1987], *Hannah et al.* [2002], *Kutterolf et al.* [2008a], *Szymanski et al.* [2013], and *Stoppa* [2015]. See Figure 2 for tephra acronyms and MP = ignimbrite close to Meco Plantel Bagaces; UCanal and LCanal = upper and lower flow units of the Canal/Tenorio ignimbrite; LEI = La Ese Ignimbrites; Papa = Papagayo Tuff). Data are averages of all analyses made for each tephra and bars represent the respective compositional range. Graph panels are repeated for clarity due to the large number of tephra layers. (a) Marine and terrestrial tephras <600 ka; (b) marine and terrestrial tephras of La Ese Ignimbrites; (c) marine and terrestrial tephras between 1 and 1.5 Ma; (d) marine and terrestrial tephras around 1.6 Ma; (e) marine and terrestrial tephras >2 Ma.
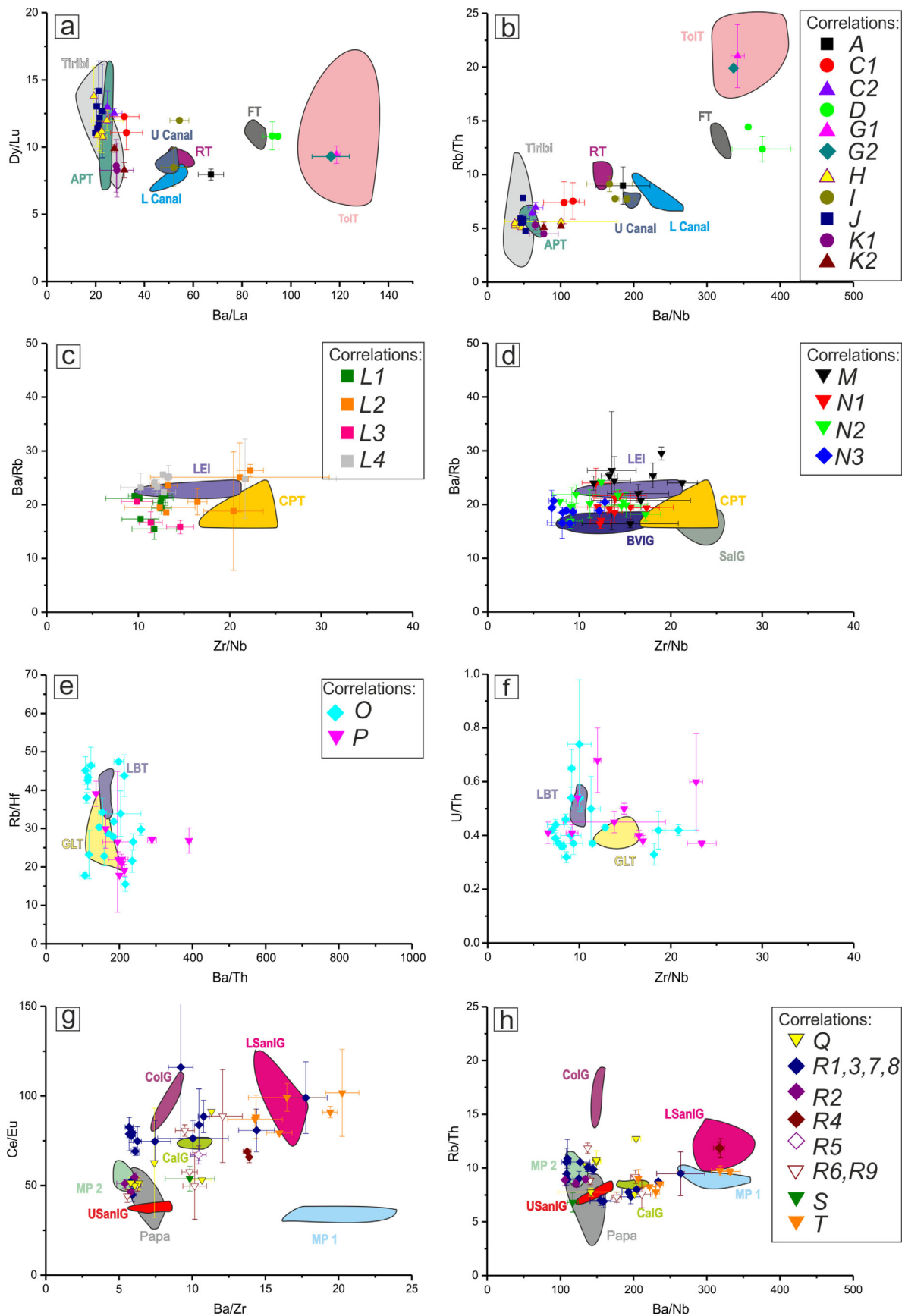
4.3.1. Costa Rican Provenance
4.3.1.1. Barva Volcano/Caldera

The Proto-Barva edifice was built between 1.2 and 0.89 Ma and was followed by the Paleo-Barva between 0.57 and 0.4 Ma and the recent Barva Volcano (Figures 1 and 2) [*Alvarado and Gans*, 2012]. Barva Volcano experienced caldera collapses at 0.5–0.49, 0.44, and 0.32 Ma that correlate with three larger and several smaller ignimbrites, namely the Bajo La Hondura Tuff (0.501 ± 0.01 Ma), the Puente de Mulas Tuff (0.439 ± 0.025 Ma), and the Tiribí Tuff (0.322 ± 0.002 Ma), the largest Costa Rican eruption in the last 350 ka [*Alvarado and Gans*, 2012]. The trachytic Tiribí Tuff has a unique chemical composition (high Zr, Nb/Rb, and low Ba/La) [*Hannah et al.*, 2002; *Pérez et al.*, 2006] that facilitates correlation with the marine tephra layer *H* (Figures 5a, 6a, 6b, S1, and S2). The occurrence of tephra layer *H* in Holes 1039B, 1241A+B, 1242A-D, U1381C, and U1414A (Figure 9) significantly extends the known dispersal area of this major eruption from Costa Rica.

Tephra layer *J* (six ash beds in Holes 1241A, 1242A-D, and U1381C) major and trace element compositions and isotope data fit the Tiribí-like Paleo-Barva compositions (Figures 5a, 6a, 6b, 7, S1, and S2) and the calculated ages (480–550 ka) match the age of the Bajo La Hondura Tuff [*Alvarado and Gans*, 2012].

Four widespread marine tephra layers (*s14*, *s17*, *s18*, *s20*; Figures 7, S3, and 9 and Table 3) imply that four eruptions similar in size to the Tiribí Tuff occurred between 0.65 and 1.15 Ma. Moreover, five additional ash beds (Sites U1379, 1242, and 1039 between 0.45 and 1.42 Ma) with a characteristic "Barva"-signal in major and trace elements (Figure 8) complement a marine assemblage that represents a total of up to eleven large eruptions from the Barva volcanic complex until ∼1.4 Ma (Interval *U1378B-36X-CC, 33–35 cm*), much more than have yet been recognized on land.

Additionally, the marine tephra layers *s17* or *s18* (0.90–1.03 Ma; 0.95–1.07 Ma) fit the dacitic composition of a 0.859 ± 0.003 Ma old ignimbrite in the Valle Central near Irazú volcano, the so-called San Jerónimo ignimbrite, described by *Alvarado et al.* [2007] and *Alvarado and Gans* [2012].

4.3.1.2. Poás Volcano

The complex stratovolcano Poás in the Cordillera Central (Figures 1 and 2) evolved during the last 1 Ma [*Sáenz*, 1982; *Prosser and Carr*, 1987; *Ruiz et al.*, 2010]. Only bulk rock analyses [*Prosser and Carr*, 1987; *Ruiz et al.*, 2010] are available for the Poás deposits so that correlation with our marine glass compositions remains uncertain. However, compositions of the two marine tephra layers (*C1* and *C2*) fit compositions at Poás Volcano fairly well. The older *C2* (Site 1039) is correlated with the Poás Lapilli Tuff (Poás LT in Figures 5a, 6a, 6b, and 9), which is probably older than 40,000 years [*Prosser and Carr*, 1987; *Gazel and Ruiz*, 2005]. Layer *C1* (Sites U1381, U1412, and U1413) may represent the low-Ti component of Poás described in *Gazel and Ruiz* [2005].

Chemical signatures of one widespread marine tephra layer (*s2*; Sites U1378, U1413; ∼80 ka), as well as three locally restricted marine ash beds in Site U1378 at ∼190 ka and at ∼450 ka, and in Site U1414 at ∼370 ka suggest a central Costa Rican origin (Figures 8 and 9). They do not show the typical "Tiribí" composition, but are similar in composition to the tephras *C1* and *C2*, and therefore may be associated with older eruptions from Poás volcano.

4.3.1.3. Platanar and Porvenir Volcanoes

The present Platanar and Porvenir volcanoes (<0.2 Ma) have grown inside the older Chocosuela Caldera (0.58–0.44 Ma) which is the origin of the Alto Palomo pyroclastic flow units comprising the Upper and Lower Alto Palomo Tuffs (0.44 ± 0.01 Ma to 0.582 ± 0.02 Ma) [*Alvarado and Gans*, 2012; *Villegas*, 2004]. These contain a series of poorly welded, ash-rich (>90%), feldspar and hornblende-bearing dacitic to rhyolitic pumice flows with unusual LREE enrichment [*Alvarado and Carr*, 1993].

We were able to correlate tephra layers *K1* and *K2* (Figures 5a, 6a, 6b, 9, S1, and S2; Sites 1039, U1412, and U1414) to the Upper and Lower Alto Palomo Tuffs by geochemical fingerprinting as well as modal composition (abundant mica and amphibole crystals). The two distinct primary tephra layers at Sites U1414 and 1039 clearly indicate two independent eruptions separated by marine sediments. In addition, we identified a marine tephra layer in Sites U1412 and U1381 (*s12*; 0.5–0.6 Ma, Figures (7 and 9), and S3 and Table 3)
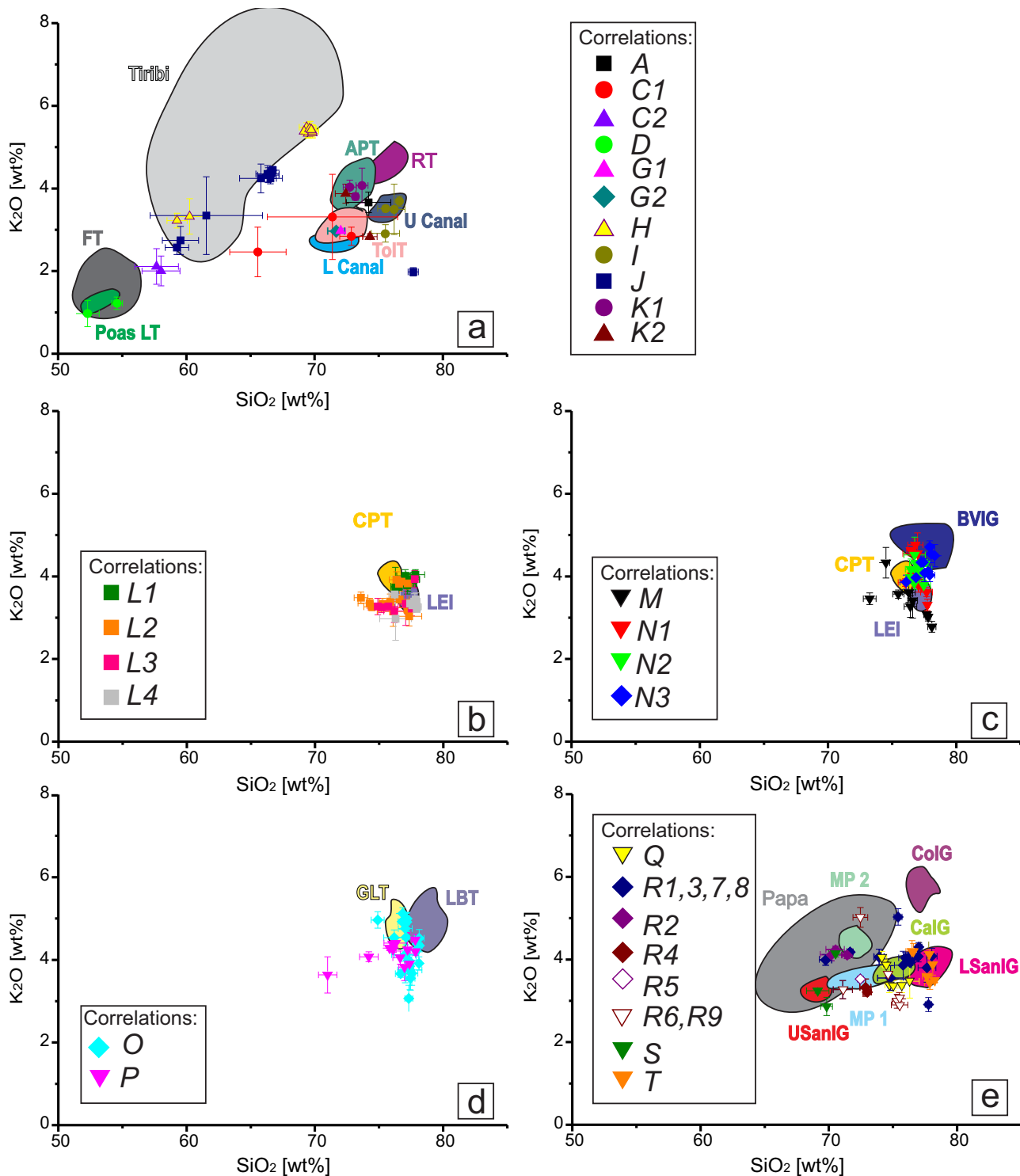

Figure 6. Glass shard compositions of marine ash beds (*A* to *T*), compared with glass-composition fields of known Holocene to Pliocene tephras on land. Our data for terrestrial eruptions is complemented by data from *Hannah et al.* [2002], *Kutterolf et al.* [2008a], *Szymanski et al.* [2013], and *Stoppa* [2015]. See Figure 2 for tephra acronyms and MP = ignimbrite close to Meco Plantel Bagaces; UCanal and LCanal = upper and lower flow units of the Canal/Tenorio ignimbrite; LEI = La Ese Ignimbrites; Papa = Papagayo Tuff. Data are averages of all analyses made for each tephra and bars represent the respective compositional range. (a, b) Marine and terrestrial tephras <600 ka; (c) marine and terrestrial tephras of La Ese Ignimbrites; (d) marine and terrestrial tephras between 1 and 1.5 Ma; (e, f) marine and terrestrial tephras around 1.6 Ma; (g, h) marine and terrestrial tephras >2 Ma.

Table 2. 39 Marker Tephra Layers With Selected Major and Trace Elements, Called Tephra Layers *A–T* With Subdividing Numbers, That Correlate Between the Different Drill Sites (Comprising 226 Individual Ash Beds) and With Volcanoes or Specific Tephras or Tephra Formations on Land[a]

	Interval	Age (Ma)	K_2O (wt %)	SiO_2 (wt %)	Ba/La	Rb/Hf	La/Nb	Zr/Hf	On Land Tephra Correlation
A	344-U1413B-1H-1, 9–11 cm	0.0011	3.66	74.15	67.21	22.78	2.74	42.65	Rinóon de la Vieja Tephra
B1	334-U1378B-4H-5, 51–53 cm	0.0360	2.15	77.35	87.36	25.57	3.45	35.28	Terra Blanca 4
B2	170-1040C-27R-5-60-61 AV	0.7970	3.30	74.04	92.66	12.90	3.18	35.43	A3/A5-Tephra
C1	344-U1413A-1H-4, 16–18 cm	0.0330	2.84	72.81					Poás
C1	344-U1412B-1H-3, 33–35 cm	0.0163	3.31	71.34	31.73	12.25	3.73	40.36	
C1	344-U1381C-1H-5, 15–17 cm	0.0407	2.46	65.54	32.63	10.33	3.19	38.00	
C2	170-1039A-1H-5, 121–130 cm	0.0870	2.11	57.66	27.58	14.87	2.38	37.66	Poás Lapilli Tuff
C2	170-1039B-2H-3, 62–68 cm	0.0679	2.00	58.00	24.78	15.35	2.47	40.19	
D	344-U1381C-2H-1, 97–99 cm	0.0600	0.97	52.29	92.32	7.77	4.06	34.16	Fontana Tephra
D	205-1254A-15R-4, 69–70 cm	0.0488	1.22	54.58	94.63	9.58	3.76	37.11	
E	170-1039A-1H-5, 121–130 cm	0.0870	4.28	77.52					Los Chocoyos
E	138-844A, 1H-1, 19–24 cm	0.0169	4.01	77.87	71.42	71.20	2.09	25.72	
E	138-844B-1H-1, 115–120 cm	0.0843	4.04	78.20					
E	138-844B-1H-1, 121-128- cm	0.0850	3.98	77.83	73.15	67.75	2.04	23.34	
E	202-1241A-1H-2, 9–14 cm	0.0924	4.00	77.98	81.88	88.01	1.96	25.49	
E	202-1241A-1H-2, 12–15 cm	0.0948	4.01	78.23	68.93	67.74	2.22	24.06	
E	205-1255A-3R-3, 54–57 cm	0.0840	3.93	77.78	67.45	64.31	2.36	25.90	
E	205-1254-16R-4, 0–1 cm	0.1057	3.98	77.59	77.40	61.46	1.96	23.72	
E	138-844A-1H-3, 0–30 cm	0.2319	3.88	78.03					
F	334-U1378B-8H-4, 110–112 cm	0.1910	4.15	75.12	34.39	38.60	2.22	32.53	L-Fall Tephra
F	202-1242A-3H-6, 59–64 cm	0.2264	4.21	75.11					
G1	170-1039B-4H-2, 56–58 cm	0.2784	2.97	71.98	118.67	11.11	2.88	35.77	Tolapa Tephra
G2	170-1040C-25R-5, 77–80 cm	0.3870	3.05	77.34	116.22	10.40	2.91	35.99	La Fuente Tephra
H	202-1242A-4H-6, 73–77 cm	0.3217	5.33	69.45					Tiribí Tuff
H	202-1242A-4H-6, 79–81 cm	0.3220	5.34	69.78					
H	202-1242A-4H-6, 79–81 cm	0.3220	5.42	69.59	24.65	14.86	3.81	44.16	
H	344-U1414A-8H-5, 40–42 cm	0.3220	5.39	69.76					
H	344-U1414A-8H-5, 45–47 cm	0.3220	5.34	69.57	21.67	13.10	1.75	43.44	
H	344-U1414A-8H-4, 98–100 cm	0.3220	5.40	69.57					
H	344-U1414A-8H-4, 105–113 cm	0.3220	5.39	69.73	21.80	13.36	1.71	43.97	
H	344-U1414A-8H-5, 3–5 cm	0.3220	5.48	69.33	21.76	13.18	1.75	43.75	
H	170-1039B-4H-4, 117–121 cm	0.3220	5.47	69.59	20.67	13.17	1.99	42.66	
H	344-U1381C-3H-7, 14–19 cm	0.3220	5.38	69.14	22.54	13.34	1.66	42.31	
H	202-1241A-2H-2, 41–43 cm	0.3229	5.39	69.46					
H	202-1241B-1H-5, 75–79 cm	0.3233	3.22	59.25	19.26	12.51	2.42	44.22	
H	202-1241B-1H-5, 75–79 cm	0.3233	5.45	69.60	20.32	13.47	1.99	43.54	
H	202-1241A-2H-2, 30–46 cm	0.3243	5.38	69.79					
H	202-1242B-5H-1, 26–30 cm	0.3298	3.32	60.23	22.83	12.45	1.94	42.39	
H	202-1242D-3H-3, 16–20 cm	0.3207	5.44	69.55					
H	202, 1242C-4H-6, 103–112 cm	0.3244	5.42	69.69					
I	344-U1414A-9H-3, 139–141 cm	0.4007	2.91	75.46	54.30	24.56	3.51	35.89	Upper Canal/Tenorio Ignimbrite (CR13-15)
I	344-U1412A-13H-1, 92–93 cm	0.4460	3.69	76.55	51.99	27.55	3.26	33.34	
I	334-U1378B-14H-3, 31–34 cm	0.4319	3.51	75.48	59.40	19.84	2.94	34.10	
I	202-1242A-5H-3, 46–47 cm	0.3688	3.49	76.14					
J	202-1242A-6H-5, 13–15 cm	0.4917	4.24	66.52					Bajo La Hondura Tuff
J	202-1242A-6H-6, 54–59 cm	0.5113	4.44	66.70	21.23	12.45	2.29	40.26	
J	202-1242A-6H-6, 55–60 cm	0.5114	3.34	61.53	21.65	13.60	2.27	41.80	
J	202-1241A-2H-4, 108–112 cm	0.4986	2.74	59.52					
J	202-1241A-2H-4, 107–117 cm	0.5010	2.57	59.24	22.63	19.32	2.15	41.99	
J	202-1242D-5H-1, 58–60 cm	0.4930	4.37	66.62	20.27	13.14	2.31	44.75	
J	202-1242D-5H-1, 50–60 cm	0.4930	4.32	66.35					
J	202-1242C-6H-4, 114–124 cm	0.4933	4.35	66.29	21.00	13.45	2.09	41.98	
J	202-1242B-6H-7, 55–65 cm	0.4979	4.42	66.64	21.21	12.30	2.18	42.01	
J	344-U1381C-5H-2, 130–132 cm	0.5004	4.24	65.78	20.38	10.69	2.56	38.18	
K1	344-U1414A-11H-2, 70–72 cm	0.5698	4.03	72.69	24.76	15.31	2.66	37.80	Upper Alto Palomo Tuff
K1	170-1039B-5H-3, 129–133 cm	0.5200	3.80	73.12	28.39	16.90	2.30	39.25	
K1	344-U1412A-15H, 3–7–9 cm	0.5200	4.07	73.64					
K2	344-U1414A-11H-3, 25–27 cm	0.5800	3.87	72.37	27.67	15.81	2.79	43.74	Lower Alto Palomo Tuff
K2	170-1039B-5H-6, 135–139 cm	0.5797	2.83	74.25	31.77	21.38	3.16	37.42	
L1	202-1242A-8H-1, 102–106 cm	0.6317	3.92	77.56	67.69	34.33	3.36	36.58	Upper La Ese Ignimbrites
L1	202-1242A-8H-1, 101–105 cm	0.6320	3.85	77.14					
L1	344-U1412A-17X-4, 28–31 cm	0.6340	4.04	77.71	55.73	33.61	3.36	32.10	
L1	344-U1412A-4X-1, 72–73 cm	0.6285	4.01	76.92	60.00	28.37	3.66	32.76	
L1	170-1039B-6H-3, 53–58 cm	0.6340	3.76	76.42	51.77	24.32	3.72	34.69	
L1	202-1242D-6H-3, 118–126 cm	0.6163	3.78	77.08					
L1	202-1242D-6H-3, 120–125 cm	0.6163	3.84	76.94	69.79	32.96	2.82	34.59	

Table 2. (continued)

	Interval	Age (Ma)	K$_2$O (wt %)	SiO$_2$ (wt %)	Ba/La	Rb/Hf	La/Nb	Zr/Hf	On Land Tephra Correlation
L1	202-1242C-7H-7, 49–53 cm	0.6165	3.82	77.10	71.92	27.80	3.33	32.38	
L1	202-1242B-8H-2, 25–28 cm	0.6156	3.92	77.06					
L1	344-U1381C-5H-6, 72–75 cm	0.6248	3.73	76.15	59.55	25.21	3.11	36.12	
L1	334-U1379C-26X-5, 133–139 cm	0.6340	3.93	77.57	58.20	31.46	3.25	29.31	
L2	344-U1381C-5H-7, 41–42 cm	0.6517	3.44	76.49	65.60	15.74	3.38	38.16	
L2	344-U1381C-5H-7, 59–60 cm	0.6648	3.03	77.22	69.12	14.62	3.01	36.00	
L2	170-1039B-6H-5, 25–26 cm	0.7143	3.19	77.11	62.53	14.57	3.60	37.89	
L2	202-1242A-8H-5, 62–67 cm	0.6881	3.39	75.75	60.34	25.06	3.49	33.09	
L2	202-1242A-8H-5, 68–69 cm	0.6887	3.26	74.33	71.43	24.44	3.01	35.83	
L2	202-1242C-8H-4, 8–10 cm	0.6653	3.33	75.17					
L2	202-1242B-8H-5, 133–138 cm	0.6656	3.35	74.15	56.20	23.56	2.53	39.31	
L2	202-1242C-8H-4, 7–10 cm	0.6653	3.15	75.97					
L2	334-U1378B-20X-3, 26–29 cm	0.6457	3.82	76.44					
L2	334-U1378B-20X-3, 39–41 cm	0.6464	3.87	76.62					
L2	334-U1412B-7X-3-27–32 cm	0.6520	3.48	73.48	56.64	18.62	3.92	39.32	
L2	334-U1378B-20X-3, 51–53 cm	0.6470	3.92	76.23					
L2	344-U1412B-7X-CC, 24–28 cm	0.6672	3.83	77.12	61.50	24.07	3.55	37.11	
L2	334-U1381A-6R-1, 38–40 cm	0.6520	3.94	77.42	66.58	24.06	3.32	26.40	
L3	334-U1378B-20X-4, 6–9 cm	0.6520	3.87	76.56	55.03	32.31	3.09	42.81	
L3	344-U1381C-5H-CC, 26–28 cm	0.6928	3.27	74.78					
L3	344-U1381C-5H-7, 66–67 cm	0.6710	3.22	77.42	71.81	32.27	2.72	32.90	
L3	202-1242A-8H-5, 127–131 cm	0.6946	3.16	76.07					
L3	202-1242C-8H-4, 82–83 cm	0.6718	3.25	75.07					
L3	202-1242C-8H-4, 82–83 cm	0.6718	3.27	75.62					
L3	202-1242A-9H-4, 120–122 cm	0.7747	3.93	77.67	72.47	37.66	2.62	37.07	
L4	344-U1381C-6H-1,31–33 cm	0.7224	2.97	76.17	68.44	16.52	2.84	41.57	Lower La Ese Ignimbrite
L4	344-U1412B-8X-1, 40–42 cm	0.8900	3.26	77.84	63.45	21.63	3.14	36.47	
L4	170-1040C-27R-5, 99–101 cm	0.8082	3.56	76.09	68.50	29.24	3.07	32.68	
L4	202-1242D-8H-1, 91–94 cm	0.7880	3.34	77.57	68.49	22.45	3.09	34.31	
L4	202-1242D-8H-1, 92–94 cm	0.7880	3.44	77.74					
L4	202-1242A-10H-2, 142–145 cm	0.8420	3.40	77.74	64.52	22.53	3.26	35.35	
L4	202-1242B-10H-1, 53–55 cm	0.7876	3.39	77.63	64.46	26.78	3.17	37.16	
L4	202-1242B-10H-1, 57–59 cm	0.7880	3.30	77.46					
L4	170-1039B-7H-2, 120–125 cm	0.8900	3.34	77.30	67.92	26.15	2.74	39.32	
L4	344-U1381C-6H-2, 93–95 cm	0.8903	3.21	77.82	70.61	26.28	2.73	38.26	
L4	344-U1381C-6H-2, 101–103 cm	0.8973	3.34	77.66	69.01	24.24	2.91	34.16	
M	170-1040C-29R-2, 56–59 cm	1.2894	4.33	74.44	50.96	12.79	2.85	40.24	Caída Pumice
M	170-1040B-6X-2, 72–77 cm	1.1800	3.06	75.73	85.87	11.73	2.73	35.09	
M	334-U1378B-27X-1, 80–83 cm	1.1666	3.08	77.62	66.35	14.55	3.02	36.73	
M	334-U1378B-27X-3, 17–21 cm	1.1800	3.61	76.21	56.72	28.00	5.28	34.01	
M	334-U1379C-47X-5, 84–1102 cm	1.1820	3.27	76.34	49.69	19.51	3.57	34.72	
M	334-U1379C-47X-4, 2–8 cm	1.1777	3.41	76.51	63.12	27.68	3.02	35.75	
M	334-U1379C-47X-4, 137–143 cm	1.1800	3.57	75.40	57.37	21.06	3.64	35.97	
M	344-U1414A-13H-5, 21–24 cm	1.1799	3.46	73.17	67.65	23.46	3.50	32.81	
M	170-1039B-8H-5, 40–44 cm	1.1726	2.78	78.01	63.05	20.18	3.19	33.64	
M	170-1039B-8H-5, 75–80 cm	1.1801	3.02	77.72	61.63	24.26	3.05	35.65	
N1	344-U1381C-6H-4, 109–111 cm	1.2017	3.62	77.60	55.89	21.86	2.92	34.43	Buena Vista Ignimbrites
N1	334-U1378B-30X-2, 43–47 cm	1.3436	4.48	76.77	61.35	27.87	2.98	30.62	
N1	334-U1378B-30X-3, 98–101 cm	1.3600	3.31	77.66	64.31	24.14	2.95	35.76	
N1	170-1039B-8H-6, 33–35 cm	1.2033	4.01	76.49	64.15	27.19	2.65	37.09	
N1	170-1039B-9H-1, 51–57 cm	1.2500	3.77	77.20	62.85	25.01	2.47	41.06	
N1	334-U1378B-31X-CC, 14–21 cm	1.3749	4.63	76.38	53.49	32.63	3.55	35.75	
N1	344-U1414A-13H-5, 92–93 cm	1.2681	3.89	76.70	60.25	25.03	3.41	35.02	
N1	344-U1414A-13H-5, 135–137 cm	1.2530	3.85	75.94	62.42	25.54	3.15	38.21	
N1	334-U1378B-32X-4, 53–54 cm	1.3796	4.76	76.73	65.68	19.51	2.83	32.70	
N1	334-U1379C-58X-3, 93–98 cm	1.3600	4.55	76.90	52.48	19.98	3.40	37.60	
N1	170-1039B-9H-1, 79–81 cm	1.2604	3.78	76.97					
N2	344-U1412D-2R-3, 85–87 cm	1.3500	3.78	77.37	67.60	37.05	2.43	36.26	
N2	344-U1413A-20X-7, 131–132 cm	1.3099	4.09	77.36	54.28	23.81	2.49	32.02	
N2	344-U1381C-6H-5, 73–75 cm	1.3134	4.07	77.06	42.68	19.31	2.41	40.42	
N2	170-1039B-9H-3, 60–62 cm	1.3660	3.98	76.40	59.82	31.20	2.60	35.78	
N2	170-1039B-9H-3, 23–27 cm	1.3522	4.17	76.38	55.90	28.05	2.39	31.45	
N2	344-U1414A-13H-6, 69–71 cm	1.3075	3.83	76.64	59.30	30.77	3.22	35.82	
N2	334-U1378B-37X-3, 8–9 cm	1.4293	4.30	77.49	55.85	24.23	2.88	47.74	
N2	334-U1378B-40X-5, 79–83 cm	1.4534	4.17	77.44	46.85	18.46	3.28	36.31	
N2	334-U1378B-38X-2, 37–38 cm	1.4331	4.52	76.67	62.55	23.55	2.80	38.43	
N2	334-U1378B-39X-7, 9–15 cm	1.4461	4.24	77.18	71.53	21.82	2.67	34.14	
N2	334-U1378B-39X-CC, 33–38 cm	1.4469	4.32	76.78	47.58	23.35	3.20	48.18	

Table 2. (continued)

	Interval	Age (Ma)	K$_2$O (wt %)	SiO$_2$ (wt %)	Ba/La	Rb/Hf	La/Nb	Zr/Hf	On Land Tephra Correlation
N2	334-U1378B-40X-5, 55–59 cm	1.4531	4.16	76.74	65.52	21.52	2.79	36.18	
N3	344-U1414A-13H-6, 79–83 cm	1.3153	3.86	76.01	66.31	27.00	2.78	33.51	
N3	202, 1242B-18H-2, 25–35 cm	1.4233	4.54	77.95					
N3	202-1242A-18H-3, 117–122 cm	1.4375	4.50	78.23	63.75	39.76	2.73	33.59	
N3	202-1242A-18H-3, 116–122 cm	1.4377	4.71	77.85	63.24	36.98	2.71	32.47	
N3	344-U1381C-6H-5, 78–80 cm	1.3183	3.97	76.77	52.35	35.30	2.57	35.36	
N3	344-U1413A-20X-8, 20–22 cm	1.4343	4.03	77.85	55.85	37.56	2.70	35.01	
N3	344-U1413A-20X-8, 24–29 cm	1.4560	4.08	77.45	74.04	32.33	2.15	30.06	
N3	170-1040C-29R-2, 109–114 cm	1.2904	4.34	77.34	68.31	36.35	2.62	32.75	
N3	170-1039B-9H-7, 42–46 cm	1.5415	4.12	77.71	65.20	36.30	2.80	34.44	
N3	334-U1378B-40X-7, 26–31 cm	1.4560	4.34	77.17	60.22	25.85	3.02	37.32	
O	344-U1412C-9R-2, 11–16 cm	1.5950	4.38	77.92	68.54	43.85	2.56	36.51	Liberia Tuff
O	334-U1379C-60X-7, 41–43 cm	1.5950	4.53	76.12	47.80	17.89	3.82	36.28	
O	206-1256B-3H-2, 34–36 cm		4.22	77.85					
O	138-844B-3H-6, 103–120 cm	1.5950	4.12	76.98					
O	170-1040C-30R-1, 91–93 cm	1.5703	4.96	74.84	52.06	23.28	2.98	38.10	
O	170-1040C-30R-1, 105–107 cm	1.5750	4.54	77.05	70.94	47.51	3.03	31.07	
O	U1378B-43X-6, 13–15 cm	1.5600	4.11	76.96	63.91	22.88	2.49	34.68	
O	170-1040C-30R-2, 87–91 cm	1.6190	4.75	76.98	52.30	42.63	2.50	37.40	
O	344-U1381C-6H-7, 60–62 cm	1.5945	3.55	77.39	69.57	21.65	3.17	26.68	
O	344-U1381C-6H-CC, 0–2 cm	1.5984	3.75	77.34	71.84	29.82	3.03	30.89	
O	U1378B-45X-1, 145–147 cm	1.5950	3.91	78.06	67.48	34.32	2.28	36.58	
O	344-U1412D-2R-4, 143–145 cm	1.5941	4.34	78.08	67.40	33.95	2.56	32.56	
O	344-U1413A-21X-3, 4–6 cm	1.5950	3.84	77.33	67.71	27.93	2.36	36.93	
O	344-U1414A-14H-3, 12–14 cm	1.5952	3.99	77.22	71.09	30.44	2.84	34.64	
O	344-U1413A-21X-3, 6–8 cm	1.5950	3.67	77.50	70.20	31.91	2.41	35.79	
O	170-1041A-11X-3, 0–2 cm	1.5972	4.52	78.07	68.51	28.80	2.42	35.30	
O	202-1242A-22X-1, 114–121 cm	1.6011	5.12	76.79	46.28	44.89	2.75	42.13	
O	202-1242A-22X-1, 115–122 cm	1.6015	4.99	77.12	53.63	43.42	2.47	34.93	
O	202-1242B-21X-6, 13–14 cm	1.6531	4.91	77.10	55.77	46.49	2.36	38.96	
O	202-1242B-21X-CC, 14–19 cm	1.5881	4.92	76.75	51.40	38.09	2.65	38.39	
O	170-1039B-10H-1, 29–44 cm	1.5950	3.66	76.62	57.36	15.59	2.94	36.86	
O	170-1039B-10H-1, 119–121 cm	1.6183	3.06	77.26	67.42	26.60	3.18	29.72	
P	334-U1379C-70X-2, 23–28 cm	1.7000	4.05	76.60	52.03	39.13	2.86	33.28	Green Layer
P	138-844B-4H-2, 130–140 cm	1.7430	4.20	77.79					
P	170-1039B-10H-5, 14–16 cm	1.7479	4.48	77.77	62.38	26.61	3.01	29.41	
P	170-1039B-10H-5, 50–54 cm	1.7573	4.40	76.24					
P	170-1039B-10H-5, 58–70 cm	1.7594	4.38	76.01	58.75	22.02	2.39	39.82	
P	334-U1378B-45X-2, 90–92 cm	1.6087	3.90	77.32	66.29	30.03	2.43	35.22	
P	170-1039B-10H-5, 81–85 cm	1.7653	4.24	76.04	52.52	17.88	2.76	39.25	
P	170-1039B-10H-5, 117–122 cm	1.7747	4.28	75.76	53.01	19.18	2.92	39.26	
P	170-1041A-11X-3, 93–94 cm	1.6190	4.07	74.15	60.16	20.96	4.14	42.57	
P	170-1041A-11X-3, 80–83 cm	1.6165	3.63	70.95	58.06	22.02	3.91	44.91	
P	344-U1412D-3R-5, 43–46 cm	1.7010	3.82	76.93	74.38	26.92	3.05	28.61	
P	202-1242B-24X-2, 10–12 cm	1.7657	4.24	77.16	72.88	26.95	3.93	29.51	
Q	334-U1378B-50X-1, 12–13 cm	2.0600	3.47	76.22	43.33	14.98	3.26	41.43	Cañas Ignimbrite
Q	170-1039B-11H-6, 116–118 cm	2.0599	3.94	74.21	47.98	13.99	3.11	39.90	
Q	202-1241B-5H-6, 112–114 cm	2.0419	3.38	74.64	57.16	16.84	3.53	39.45	
Q	202-1241A-6H-1, 15–19 cm	2.0457	3.36	74.93					
Q	170-1040C-30R-3, 45–50 cm	1.6744	3.37	75.60	64.22	18.93	3.17	41.52	
Q	170-1040C-30R-4, 108–113 cm	1.9829	3.86	74.40	48.59	13.31	3.07	38.48	
Q	344-U1414A-15H-3, 121–123 cm	2.0602	4.05	74.04	50.33	12.86	2.69	39.57	
									Bagaces Formation
R1	170-1039B-12X-2, 79–86 cm	2.1264	4.00	69.65	49.63	13.61	2.76	39.49	Río Colorado Ignimbrite
R1	344-U1414A-15H-4, 5–7 cm	2.0836	4.07	73.81	47.19	12.28	3.08	39.11	
R1	202-1241B-6H-1, 7–9 cm	2.0961	4.19	71.55					
R2	170-1040C-31R-2, 45–55 cm	2.4806	4.24	70.41	40.23	13.49	3.01	40.57	
R2	170-1039B-13X-1, 61–66 cm	2.2288	4.12	71.32	41.13	13.58	3.26	38.60	Ignimbrite at Meco Plantal MP2 (sample CR13-17)
R2	170-1039B-13X-5, 31–33 cm	2.3499	4.12	70.08	40.99	14.24	2.59	41.64	
R3	344-U1414A-15H-6, 76–78 cm	2.3391	3.56	74.70	55.24	17.67	3.50	40.65	
R3	U1378B-54X-2, 0–3 cm	2.6239	4.05	75.86	60.20	25.91	2.63	35.97	
R4	170-1040B-15X-4, 64–70 cm	2.7810	3.22	72.89	65.67	23.07	4.82	42.00	Ignimbrite at Meco Plantal MP1 (sample CR13-18)
R4	170-1040B-15X-4, 102–117 cm	2.7896	3.33	72.75	63.49	22.31	5.01	41.80	
R5	170-1040B-16X-2, 64–71 cm	2.9115	3.54	72.35	46.01	25.23	4.43	42.51	
R6	170-1041A-18X-1, 30–33 cm	2.8871	5.03	72.34	71.95	11.02	1.91	41.10	(Similar to sample CR13-20)
R6	170-1040B 17X-2, 89–94 cm	3.1518	3.28	70.98	65.49	16.68	4.06	37.63	

Table 2. (continued)

	Interval	Age (Ma)	K₂O (wt %)	SiO₂ (wt %)	Ba/La	Rb/Hf	La/Nb	Zr/Hf	On Land Tephra Correlation
R7	202-1241C-5H-2, 45–49 cm	3.1473	4.12	76.28	44.73	12.52	2.43	37.13	
R7	202-1241A-8H-5, 146–148 cm	3.1483	4.07	76.26	41.60	15.54	2.63	42.75	
R7	202-1241B-8H-5, 41–43 cm	3.1486	4.05	76.43	44.14	12.58	2.49	38.70	
R7	202-1241A-8H-5, 145–150 cm	3.1490	4.08	76.85	44.17	13.99	2.44	37.66	
R7	205-1254A-3R-3, 97–100 cm	3.2431	3.81	77.53					
R7	170-1039B-15X-1, 36–42 cm	3.3855	3.93	76.22	43.14	12.43	2.51	38.81	
R7	344-U1414A-17H-5, 124–130 cm	3.3500	3.87	75.67	49.62	14.68	2.61	35.63	
R7	170-1040C-32R-6, 18–25 cm	3.3821	5.04	75.28	43.90	34.10	2.89	36.35	
R8	334-U1378B-61X-1, 109–111 cm	3.5851	4.09	77.90	68.60	27.48	3.41	29.89	
R8	334-U1378B-62X-2, 83–85 cm	3.6668	4.31	76.90	52.80	15.51	3.71	27.31	
R8	205-1254A-3R-5, 41–45 cm	3.7287	2.92	77.64	57.14	11.80	2.53	27.19	
R9	170-1040B-20X-3, 65–70 cm	3.8380	3.06	75.37	56.71	20.61	3.72	38.64	
R9	170-1040B-20X-3, 127–132 cm	3.8511	2.91	75.40	49.10	15.78	3.61	36.54	
R9	170-1040C-1R-5, 102–123 cm	3.8647	3.00	75.21	58.99	17.84	3.43	40.73	
R9	170-1039B-15X-6, 27–29 cm	3.9647	3.64	74.51	48.86	12.18	2.88	40.14	
S	170-1039B-15X-7, 20–25 cm	4.0842	3.24	69.06	35.41		3.91		Upper Sandillal Ignimbrite
	(Data from Clift et al., 2005)								
S	84-565*-10R-7, 26–30 cm	4.0999	2.86	69.75	41.39	16.06	2.83	38.30	
S	138-844B-4H-4, 92-102–10 cm	4.1230	4.14	70.44					
T	138-844B-4H-4, 92–102 1 cm	4.1230	4.12	77.74					Lower Sandillal Ignimbrite
T	344-U1414A-18H-5, 104–108 cm	4.1501	3.87	78.01	76.33	24.24	2.71	35.82	
T	170-1039B-16X-1, 64–74 cm	4.1499	3.59	77.55	87.98	31.22	3.61	37.09	
T	170-1039B-16X-1, 100–101 cm	4.1703	3.43	77.78	82.04	25.47	4.04	39.41	
T	170-1040C-3R-1, 80–88 cm	4.1355	4.19	76.50	59.05	27.83	3.99	33.82	
T	205-1254A-5R-7, 32–36 cm	4.1343	3.49	78.16	67.04	33.08	3.31	38.44	
T	205-1254A-5R-8, 14–21 cm	4.1500	4.19	76.40	59.46	22.41	3.88	34.59	

[a]Ages are calculated with sedimentation rates or ages from literature (references are given in the text).

between *K1* and *K2* that correlates to the Platanar volcanic complex. Moreover, a marine ash bed below *K2* at site 1039 at ∼0.6 Ma (Figure 8) also has the typical Chocosuela chemistry. Hence, the marine ashes suggest there were both precursor and intermediary eruptions of the Alto Palomo Tuffs that had not yet clearly been identified on land.

4.3.1.4. Tenorio Volcano

Tenorio volcano is only known for its effusive phases between 0.74–0.54, 0.37–0.26, and 0.26–0.09 Ma [*Alvarado and Gans*, 2012] but during our fieldwork we sampled the several meters thick so-called Canal/Tenorio ignimbrite (sample CR13-15) between Miravalles and Tenorio volcano. The ignimbrite consists of two flow units; its source and age are unknown. Marine tephra layer *l* (∼0.4–0.45 Ma) agrees geochemically with samples taken from the upper part of this ignimbrite, but overlapping tephra compositions leave correlations of marine ashes to either Miravalles or Tenorio volcano ambiguous. The two marine tephra layers *s6* and *s11* (Sites U1378, 1040, and 1039), which are ∼0.25 and ∼0.39 Ma old, have very similar, although slightly different, compositions (Figures (7 and 9), and S3) that suggest their relation to these volcanoes. A ∼0.5 Ma old single marine ash bed in Site 1039 matches the first and second effusive phases of Tenorio [cf. *Alvarado and Gans*, 2012].

4.3.1.5. Miravalles, Rincón de la Vieja, and Their Precursor Systems

The stratigraphic framework in the northern part of Costa Rica with overlapping deposits from the Miravalles and the Rincón de la Vieja systems and their respective precursor calderas (Guayabo and Cañas Dulces) including Pliocene and Miocene eruptive centers of unknown locations has not yet been completely resolved but contains the two prominent Bagaces and Liberia formations (Figure 2) [*Alvarado and Gans*, 2012; *Chiesa*, 1991; *Zamora et al.*, 2004; *Alvarado et al.*, 1992; *Gillot et al.*, 1994; *Vogel et al.*, 2004]. The <8–2.02 Ma old Bagaces Formation contains the Carbonal lava flow (8.05 ± 0.09 Ma), Alto Mirador Ignimbrite (4.87 ± 0.07 Ma), Lower Sandillal Ignimbrite (4.15 ± 0.02 Ma), Upper Sandillal Ignimbrite (4.1 ± 0.02 Ma), Pan de Azúcar Ignimbrite (3.64 ± 0.066 Ma), Abomal Fall (3.21 ± 0.06 Ma), Abomal Ignimbrite (2.97 ± 0.03 Ma), Río Colorado Ignimbrite (2.08 ± 0.01Ma), and Cañas Ignimbrite (2.06 ± 0.02 Ma). The Papagayo Tuff [*Szymanski et al.*, 2013] (Papa correlation field in Figures 5e, 6g, 6h, S1, and S2), a welded ignimbrite with basal contact to the Carbonal lava flow (∼8 Ma; Figure 2) [*Alvarado and Gans*, 2012]), may correspond to the Río Colorado Ignimbrite.

The ∼1.6–0.6 Ma old Liberia Formation comprises the Green Layer (∼1.8 Ma), the Liberia Tuff dated at 1.595 ± 0.02 Ma by *Alvarado and Gans* [2012] and at 1.43 ± 0.09 Ma by *Molina et al.* [2014], the Salitral
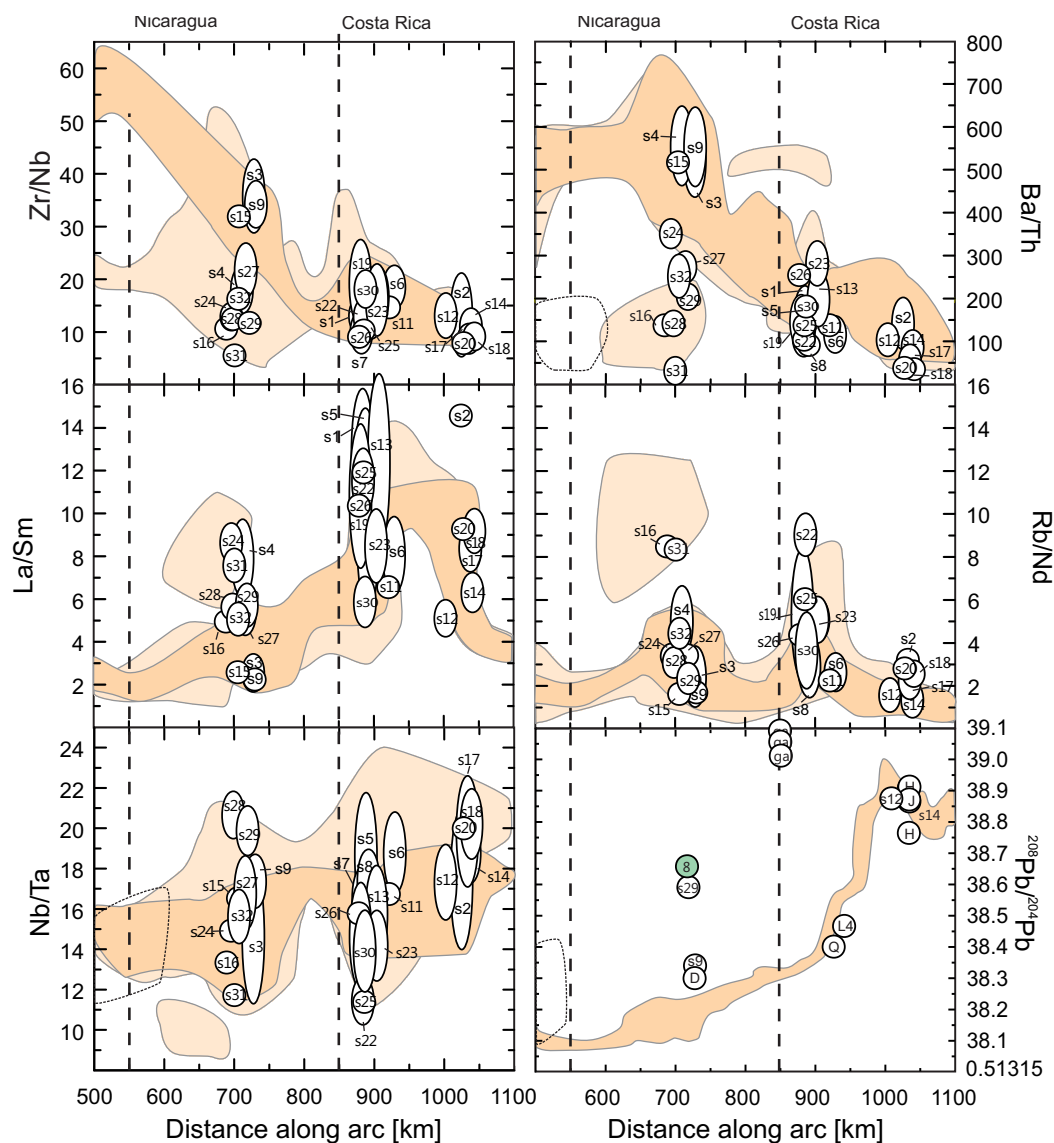
Figure 7. Comparison of glass compositions of ash beds correlated between multiple sites (tephra layers *s1–s32*) with Zr/Nb, La/Sm, Nb/Ta, Ba/Th, Rb/Nd, and ²⁰⁸Pb/²⁰⁴Pb variations along the CAVA as discussed in the text. ²⁰⁸Pb/²⁰⁴Pb variations include all obtained analyses. Light orange fields represent the Holocene volcanism along the CAVA (data from *Kutterolf et al.* [2008a] and *Stoppa* [2015]), whereas the pale fields indicate the >1 Ma along-arc variations (data for Costa Rica is published in this contribution, data for Nicaragua is unpublished). The unfilled "special compositional" field at the same position as the Nicaraguan provenance is built on data for Neogene Honduran ignimbrite deposits from *Jordan et al.* [2007b]. Green colored ellipsoid indicate marine Site U1414 where ash bed was found and ash beds are consecutively numbered from young to old.

Ignimbrite (1.36 ± 0.02 Ma), the Buena Vista Ignimbrites (1.311 ± 0.02 and 1.456 ± 0.036 Ma), Caída Pumice (1.18 ± 0.02 Ma), and the La Ese Ignimbrites (0.89 ± 0.03 to 0.620 ± 0.01 Ma).

Bagaces Formation on the Seafloor. Tephra layer *Q* comprises ash beds from five sites that were chemically correlated to the Cañas Ignimbrite (Figures 5e, 6g, 6h, 9, S1, and S2). Tephra layers *S* (at Sites 1039, 565, and 844) and *T* (at Sites U1414, 1254, 1040, 1039, and 844) compositionally correlate to the Upper Sandillal Ignimbrite and Lower Sandillal Ignimbrite, respectively (Figures 5e, 6g, 6h, S1, and S2). The compositional overlap of Bagaces Formation units between Cañas Ignimbrite and Sandillal Ignimbrites complicates correlations to individual eruptions. We found at least nine tephra layers (*R1–R9*) that fit this age interval and have glass compositions typical for the Bagaces Formation. *R1* through *R9* are found mainly in Sites 1039, 1040, and 1041 offshore the Nicoya Peninsula (Figure 9). Tephra layer *R1* has a calculated age of ~2.1 Ma that fits the age of the widely distributed Río Colorado Ignimbrite (2.08 ± 0.01 Ma) [*Alvarado and Gans*, 2012].

Table 3. Site to Site Correlations[a]

Correlation	Intervals	Age (Ma)	Provenance
s1	U1378B-3H-6, 29–30 cm, U1378B-3H-6, 33–34 cm, 205-1255A-3R-2, 30–32 cm	0.006–0.027	N-Costa Rica (870–930 km, Rincón, Miravalles, Tenorio)
s2	334-U1378B-5H-4, 106–108 cm, 344-U1413A-3H-2, 64–65 cm	0.071–0.075	C-Costa Rica (1000–1050 km, Platanar, Poás)
s3	205-1255A-3R-3, 63–65 cm, 170-1039A-2H-3, 20–25 cm, 344-U1381C-2H-3, 39–41cm, 205-1255A-3R-3, 65–69 cm, 205-1254A-16R-CC, 5–7 cm, 170-1039A-2H-3, 20–25 cm, 170-1039B-3H-2, 41–44 cm, 344-U1414A-5H-1, 106–108 cm	0.095–0.162	C-Nicaragua (680–740 km, Las Sierras)
s4	344-U1381C-2H-6, 136–138 cm, 202-1242C-3H-5, 101–103 cm, 202-1242B-3H-6, 62–64 cm	0.174–0.195	Central Nicaragua (∼700 km, Malpaisillo)
s5	344-U1413A-5H-3, 75–77 cm, 334-U1378B-9H-5, 3–5 cm, 334-U1378B-9H-5, 3–5 cm	0.216–0.249	N-Costa Rica (870–930 km, Rincón, Miravalles, Tenorio) or C-Costa Rica (1000 km, Platanar, Poás)
s6	334-U1378B-9H-5, 34–36 cm, 170-1039A-3H-3, 23–28 cm	0.251–0.262	N-Costa Rica (∼920–950 km, Tenorio, Arenal)
s7	344-U1413A-10H-7, 58–66 cm, 170-1040A-1H-5, 67–80 cm, 170-1039A-3H-3, 105–112 cm	0.272	N-Costa Rica (∼880 km, Rincón)
s8	170-1039A-3H-4, 7–13 cm, 170-1039A-3H-4, 15–19 cm, 170-1039A-3H-4, 71–75 cm, 170-1040C-25R-1, 19–26 cm, 170-1039A-3H-4, 75–77 cm	0.279–0.299	N-Costa Rica (∼880–900 km, Rincón, Miravalles)
s9	344-U1414A-8H-6, 19–20 cm, 170-1040C-25R-4, 5–8 cm	0.334–0.357	C-Nicaragua (680–740 km, Las Sierras)
s10	202-1242A-5H-3, 123–126 cm, 344-U1381C-4H-4, 0–2 cm	0.377–0.391	C-Nicaragua (680–740 km, Las Sierras)
s11	170-1039B-4H-6, 123–125 cm, 170-1040C-25R-4, 71–73 cm	0.366–0.397	N-Costa Rica (920 km, Miravalles, Tenorio)
s12	344-U1381C-5H-2, 148–150 cm, 344-U1412A-17X-3, 46–50 cm	0.505–0.620	Central Costa Rica (∼1000 km, Platanar)
s13	202-1242A-7H-6, 120–121 cm, 344-U1381C-5H-5, 93–95 cm, 170-1039B-6H-2, 106–113 cm	0.595–0.621	N-Costa Rica (∼900 km, Miravalles/Tenorio)
s14	202-1241A-2H-6,126–135 cm, 202-1241A-2H-6, 130–138 cm, 202-1242A-8H-4, 125–127 cm, 170-1039B-6H-5, 7–9 cm, 202-1241B-2H-4, 72–77 cm, 344-U1414A-12H-1, 22–28 cm	0.652–0.76	C-Costa Rica (1020–1050 km, Poás, Barva)
s15	170-1040C-27R-5, 28–30 cm, 202-1242D-7H-4, 70–78 cm	0.712–0.788	C-Nicaragua (680–740 km, Las Sierras)
s16	202-1242C-11H-1, 47–48 cm, 202-1242C-11H-1, 77–78 cm, 344-U1413A-19X-5, 70–78 cm	0.960	S-Nicaragua (750–800 km)
s17	202-1242A-11H-3, 112–126 cm, 202-1242B-11H2, 116–128 cm, 202-1241A-3H-3, 88–90 cm, 202-1242A-11H-4, 0–9 cm, 344-U1381C-6H-3, 63–65 cm, 170-1039B-7H-7, 31–37 cm	0.903–1.03	C-Costa Rica (1020–1050 km, Poás, Barva)
s18	202-1241B-3H-1, 54–56 cm, 202-1241A-3H-4, 27–33 cm, 202-1242C-11H-3, 119–132 cm, 202-1242A-11H-7, 26–31 cm, 202-1242A-11H-7, 6–20 cm, 170-1039B-8H-2, 6–14 cm	0.949–1.069	C-Costa Rica (1020–1050 km, Poás, Barva)
s19	344-U1413C-16R-6, 91–94 cm, 344-U1412C-7R-1, 102–105 cm, 334-U1378B-26X-3, 18–20 cm, 334-U1378B-26X-3, 40–42 cm, 334-U1378B-26X-3, 140–142 cm, 334-U1378B-26X-3, 105–110 cm, 334-U1379C-42X-1, 18–22 cm, 334-U1379C-42X-3, 90–110 cm, 334-U1379C-42X-4, 95–127 cm, 334-U1379C-42X-5, 31–34 cm, 334-U1378B-26X-5, 121–124 cm, 334-U1378B-26X-6, 93–96 cm, 202-1242A-12H-4, 108–109 cm, 202-1242C-12H-1, 68–70 cm	1.046–1.124	N-Costa Rica
s20	344-U1381C-6H-4, 12–14 cm, 170-1039B-8H-4, 53–67 cm	1.107–1.143	C-Costa Rica (1020–1050 km, Poás, Barva)
s21	138-844B-2H-6, 145–150 cm, 170-1041A-9X-1, 73–75 cm, 138-844B-3H-2, 13–25 cm	0.949–1.197	N-Guatemala (∼140 km, Atitlán)
s22	344-U1412D-2R-3, 88–94 cm, 202-1242C-15H-7, 22–29 cm, 202-1242B-15-CC, 14–26 cm, 202-1242A 16H-4, 130–138, 202-1242B 16H-1, 22–27 cm	1.311–1.348	N-Costa Rica (∼880 km), or N-Guatemala (140 km, Atitlán)
s23	170-1041A-10X-2, 98–102 cm, 202-1242A-19H-1, 23–32 cm, 202-1242B-19X-1, 18–22 cm	1.410–1.467	N-Costa Rica (∼880–920 km, Guayabo, Cañas Dulces)
s24	334-U1379C-60X-2, 89–94 cm, 344-U1414A-14H-1, 7–9 cm, 344-U1414A-14H-1, 31–33 cm	1.403–1.528	C-Nicaragua (690–770 km)
s25	170-1039B-11H-3, 16–20 cm, 202-1241A-5H-5, 10–15 cm	1.854–1.917	N-Costa Rica (∼880–920 km, Guayabo, Cañas Dulces)
s26	344-U1414A-15H-2, 76–79 cm, 334-U1380A-5R-5, 31–33 cm	1.980	N-Costa Rica (∼880 km, Orosí, Guayabo)
s27	170-1039B-16X-7, 0–5 cm, 170-1039B-16X-CC, 16–21 cm, 205-1254A-8R-8, 50–65 cm	4.620–4.709	C-Nicaragua (700 km)
s28	170-1039B 19X-CC, 20–26 cm, 344-U1414A-23X-5, 2–7 cm	6.271–6.389	C-Nicaragua (∼700 km)
s29	170-1039B 20X-1, 37–40 cm, 344-U1414A-24X-3, 26–32 cm, 344-U1414A-24X-3, 56–60 cm	6.291–6.725	C-Nicaragua (∼700 km)
s30	170-1041C-1R-1, 27–30 cm, 170-1041C-1R-3, 74–86 cm, 344-U1414A-24X-4, 0–3 cm	6.58–6.75	N-Costa Rica (880–930 km, Orosi, Guayabo, Cañas Dulces, Tenorio)
s31	170-1039B 20X-2 9–12 cm, 344-U1414A-24X-6, 61–63 cm, 344-U1414A-24X-6, 33–36 cm	6.359–6.902	C-Nicaragua (700 km), or Honduras
s32	170-1039B 20X-5, 121–123 cm, 344-U1414A-25X-6, 68–70 cm	6.675–7.391	C-Nicaragua (650–750 km)

[a]127 ash beds can be correlated between sites and form the 32 tephra layers called *s1–s32*. Ages are calculated using sedimentation rates.
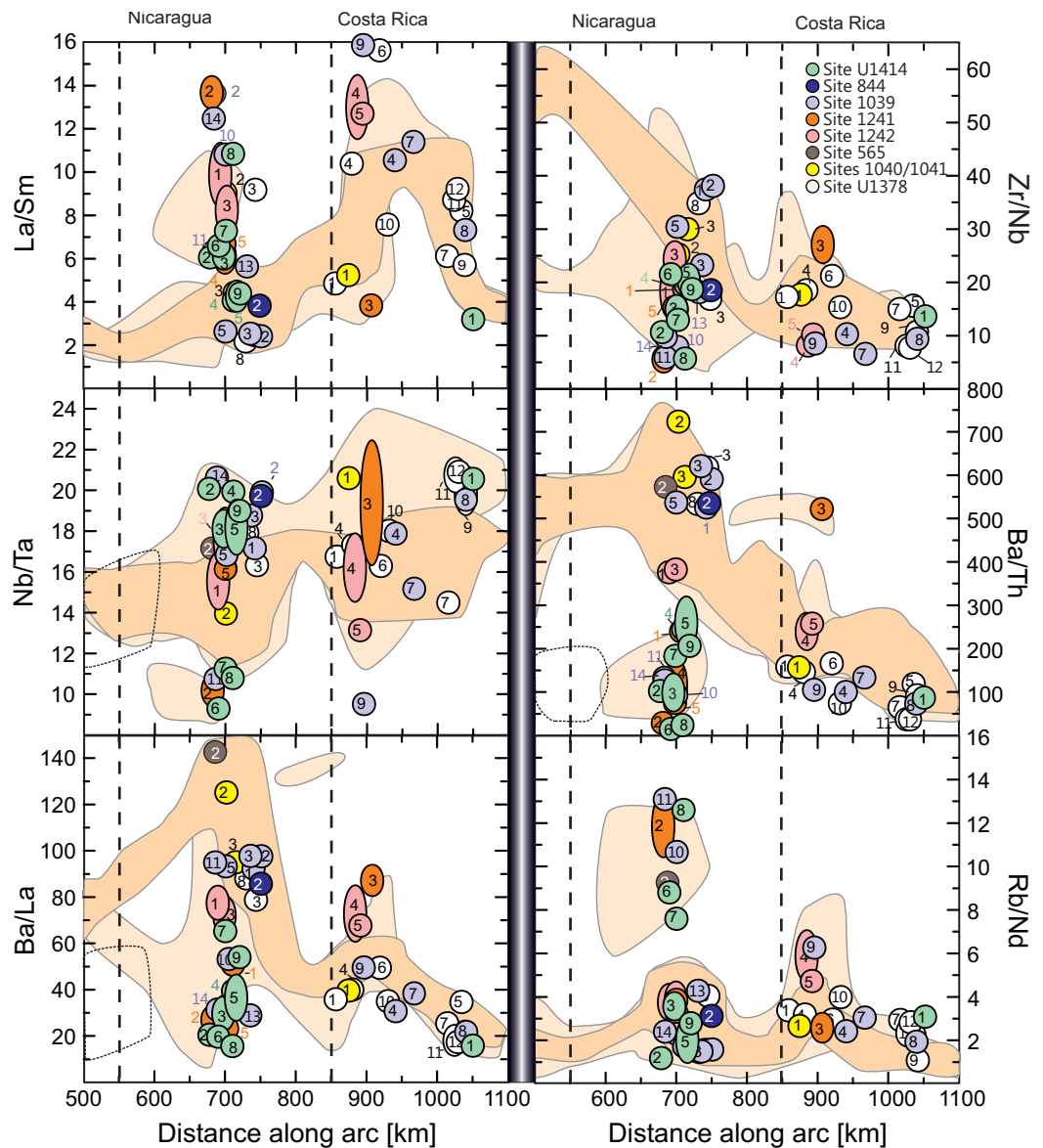
Figure 8. Comparison of glass compositions of ash beds that cannot be correlated between multiple sites with Zr/Nb, La/Sm, Nb/Ta, Ba/La, Ba/Th, and Rb/Nd variations along the CAVA as discussed in the text including the same provenance field of on-land deposits as in Figure 7. Colors of ellipsoids indicate the respective marine site where ash beds where found and ash beds are consecutively numbered from young to old.

We correlate marine tephra layers *R2* and *R4* to two ignimbrite flow units that we sampled close to Meco Plantel near Bagaces city (MP1 and MP2; Figures 5e, 6g, 6h, 9, S1, and S2), while tephra layer *R6* fits the geochemical composition of another, yet unnamed ignimbrite (sample CR13-20). The along-arc provenance plots suggest widespread tephra layer *s30* (Sites U1414 and 1041; Figures 7 and S3) also relates to the Bagaces Formation, as well as two ash beds (Intervals *170-1040C-8R-4, 3–5 cm; 170-1039B-23X-1, 15–17 cm*) between 2 and 6 Ma (Figure 8). The occurrence of at least nine Bagaces tephra layers on the seafloor that complement the number of Bagaces ignimbrites on land [e.g., *Semm and Alvarado*, 2007; *Szymanski et al.*, 2013], and the strong compositional similarity between all these deposits, suggests that the formation represents repeated large-magnitude, probably caldera-forming eruptions from a huge magma system that operated in a near-steady state from 4 to 2 Ma in northern Costa Rica.

Liberia Formation on the Seafloor. The Liberia Tuff is one of the most prominent Quaternary tephra units on land [*Chiesa*, 1991; *Alvarado and Gans*, 2012] and correspondingly its marine equivalents can be identified in 12
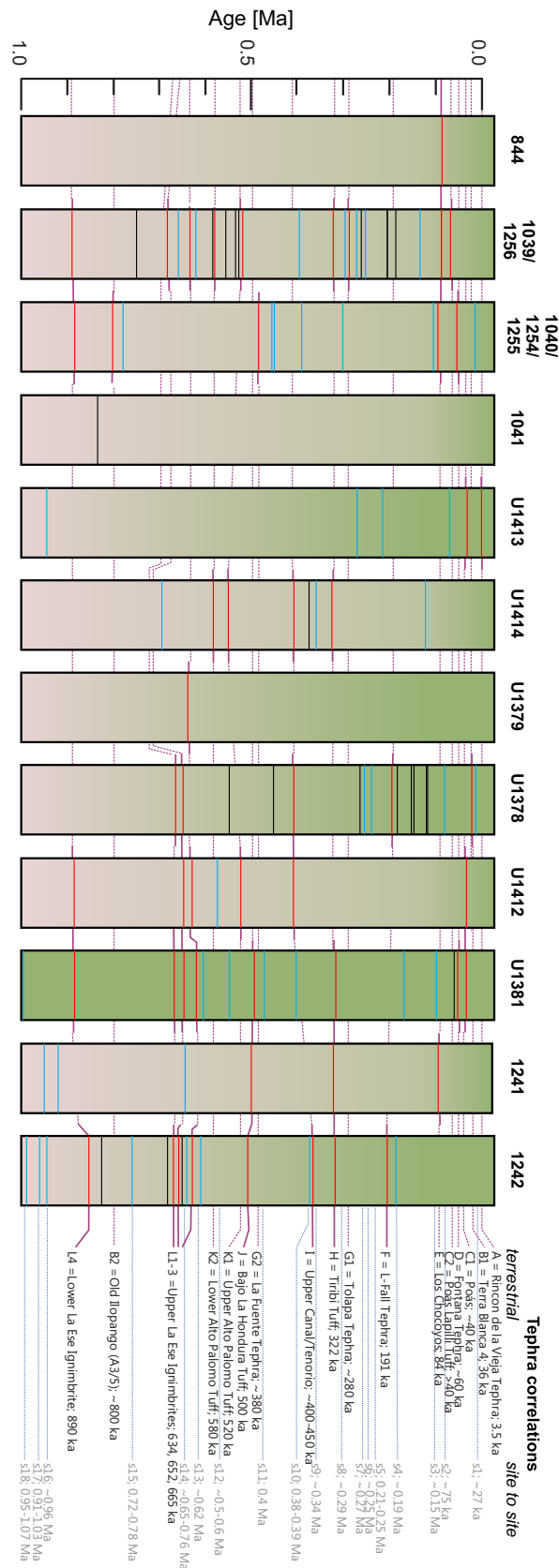
Figure 9. (continued).

marine sites (tephra layer *O*; Figures 5d, 6e, 6f, S1, S2, and 9; U1414, U1413, U1412, U1381, U1379, U1378, 1242, 1256, 844, 1041, 1040, and 1039) by chemical fingerprinting and the characteristic biotite-rich nature of the tephra layer. Closely associated to the Liberia Tuff is the "Green Layer," a thick pumice fallout below the Liberia Tuff that has similar juvenile composition (Figure 3) and has consistent sedimentation-rate-derived ages of ~1.7 Ma at all sites, which are supported by a new Ar/Ar age of 1.81 ± 0.11 Ma (*170-1039B-10H-5, 58–70 cm*; Table 1). Glass compositions from marine tephra layer *P* that occurs in seven sites (Figure 9; Sites U1412, U1379, U1378, 1242, 1041, 1039, and 844) correlate with "Green Layer" compositions (Figures 5d, 6e, 6f, S1, and S2).

Three marine tephra layers (*N1*, *N2*, and *N3*) have the geochemical signature of the Buena Vista Ignimbrite (Figures 5c, 6d, 9, S1, and S2) that presumably contains at least two flow and four fall units [*Alvarado and Gans*, 2012; *Gillot et al.*, 1994; *Chiesa et al.*, 1992; *Deering et al.*, 2007]. We did not find traces of the Salitral Ignimbrite that is of similar age (1.36 ± 0.02 Ma) as the Buena Vista Ignimbrite.

The Caída Pumice and the La Ese Ignimbrites are related to collapses of the 1.17–1.0 Ma old Guayabo Caldera that hosts the later Miravalles and Zapote volcanoes [*Alvarado and Gans*, 2012]. We found marine tephra layers with the geochemical signature of the La Ese Ignimbrites (*L1-L3* Upper La Ese, *L4* Lower La Ese; Figures 5b, 6c, S1, and S2) in seven sites (Figure 9; Sites U1412, U1381, U1379, U1378, 1242, 1040, and 1039). We distinguish four layers, *L1–L4*, because there are several distinct horizons of that composition per hole. We interpret that each of the four layers represents one eruption from Guayabo Caldera. *L1* through *L4* ages calculated from
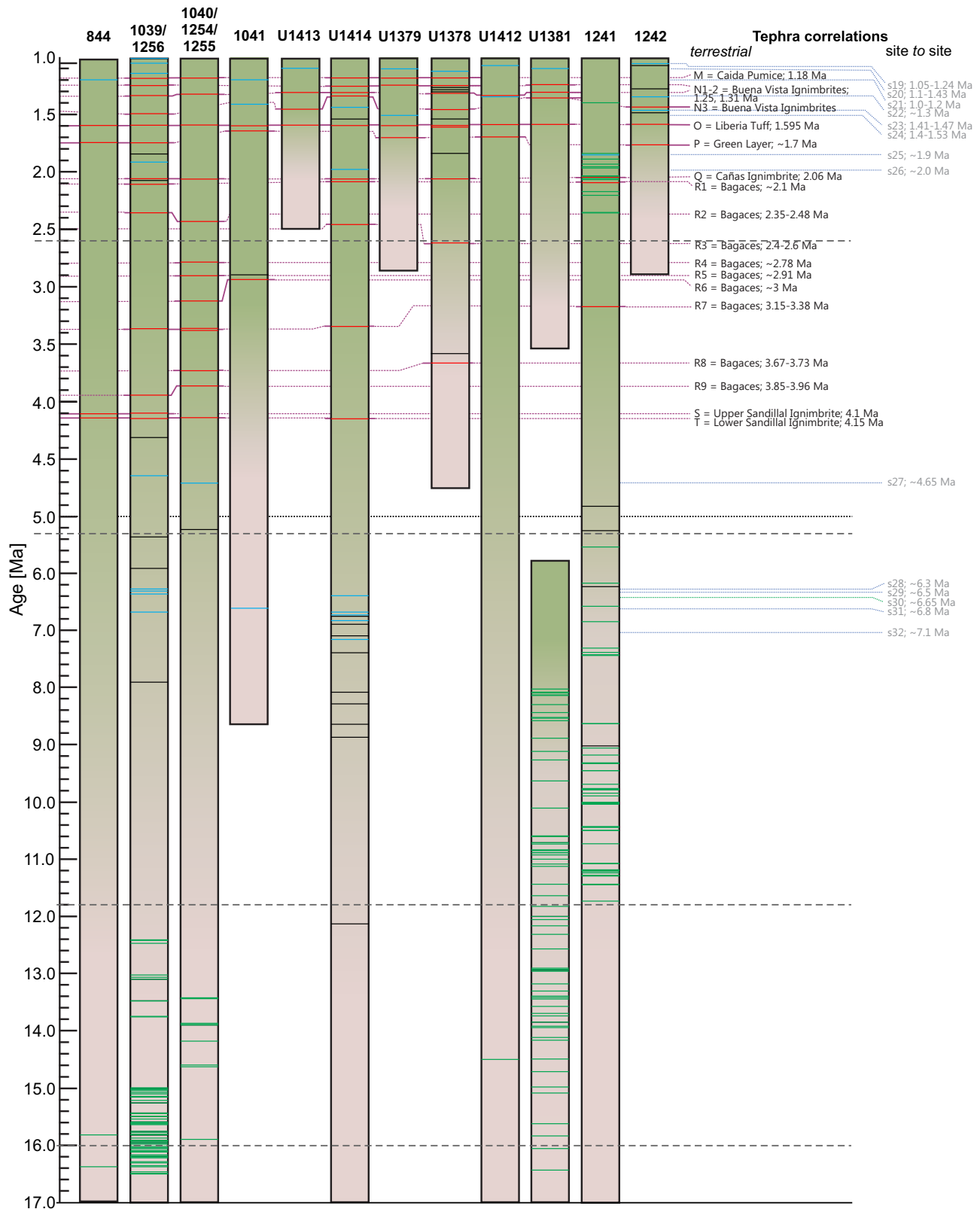
Figure 9. Compositionally correlated tephra layers *A* through *T* provide chronostratigraphic links between the 12 drill sites offshore southern CAVA arranged from South (right) to North (left). Layers *A* to *T* (red) correlate with specific tephras on land as shown in Figures 5 and 6 and Table 2. Layers *s1–s32* (blue) are correlated between the sites and to eruptive centers on land (see Table 3). Unlabeled ash beds could not be correlated (black) or have an ocean island signature (green). Dashed gray lines indicate Pliocene/Pleistocene (2.6 Ma), Late Miocene/Pliocene (5.3 Ma), Late Miocene/Middle Miocene (11.8 Ma), and Middle Miocene/Early Miocene/(16 Ma) boundaries after *Walker et al.* [2013]. Black dotted line indicates change in age scale at 5 Ma. (a) Correlations from 0 to 1 Ma; (b) correlations from 1–17 Ma.

sedimentation rates overlap completely with the Ar/Ar ages for the La Ese Ignimbrites. Our along-arc provenance analysis shows that tephra layer *s13* (~0.62 Ma) and four single marine ash beds between 0.8 and 1.85 Ma (Figure 9; Sites U1378, 1041, 1242, and 1039; Figures (7 and 8), and S3 and Table 3) have geochemical compositions similar to the La Ese Ignimbrites.

Stratigraphically deeper we found marine tephra layer *M* that we infer to probably be the equivalent of the 1.18 Ma old Caída Pumice (Figure 9). Although the chemical correlation is ambiguous (Figures 5c, 6d, S1, and S2), the stratigraphic order (Figure 2) and ages between 1.16 and 1.29 Ma, calculated with sedimentation rates, support this correlation.

Comparison with along-arc compositional variations suggests that five marine tephra layers (*s26, s25, s23, s22, s19*; *202-1242A-19H-4, 84–89 cm*; Figures 7–9 and S3; also at Sites U1414, U1412, U1413, U1378, 1039, 1041, 1241, and 1242) and one local ash bed with ages between ~1 and 2 Ma could be associated with the Cañas Dulces Caldera, a precursor to Rincón de la Vieja that destroyed and replaced the former Alcántaro Volcano (2.17–1.78 Ma) [*Alvarado and Gans*, 2012; *Molina et al.*, 2014]. Accepting that Rincón de la Viejá volcano is younger than 0.56 Ma, we can identify four tephra layers (*s8, s7, s5, s1*; *U1378B-9H-6, 88–91 cm*; also at Sites U1413, U1378, 1039, 1040, 1254; Figures 7–9 and S3 and Table 3) in the Pacific marine sediments that probably derive from this volcano. Tephra layer *A* in the uppermost centimeters of Site U1378 (Figures 5a, 6a, 6b, 9, S1, and S2) can be unambiguously correlated to the ~3.5 ka Rincón de la Vieja Tephra (RT) [e.g., *Soto et al.*, 2003].

4.3.2. Nicaraguan Provenance
Widespread tephra layer *s4* (Figure 9; Sites U1381 and 1242, ~180 ka) and seven individual marine ash beds younger than ~0.6 Ma (Figure 9; Sites 1039, U1378, 1242; Figures 7 and S3 and Table 3) have unique potassium-poor, silica-rich compositions, as well as characteristic trace element ratios that fit an origin from Central Nicaragua, most probably precursor systems of the Apoyo Caldera and Chiltepe volcanic complex. Other marine tephras relate to the following three volcanic systems.

4.3.2.1. Neogene Coyol Arc
Seven tephra layers (Figure 9; *s16, s24, s27–s29, s31*, and *s32*; Sites U1413, U1414, U1379, 1241, 1242, 1254/55, 1039, 1041, and 565) from ~1 to ~7 Ma, and 25 individual marine ash beds between ~1 and ~9 Ma, possess similar chemical compositions like pyroclastic deposits sampled from the Neogene Coyol arc (Figures (7 and 8), and S3). These compositions also agree with those of marine ash beds found in the Caribbean and stand out by trace element ratios indicative of continental crust influence on magma evolution (e.g., K/Rb, Th/Nb, Rb/Nd, Rb/Hf, Ba/La, and Ba/Th) [*Wark*, 1991; *Vogel et al.*, 2004; *Walker et al.*, 2007; *Jordan et al.*, 2006, 2007a, 2007b]. According to *Jordan et al.* [2006, 2007a, 2007b] rocks of such compositions cover the 27–4.8 Ma age range but *Saginor et al.* [2011a, 2011b] and *Alvarado et al.* [2007] imply major gaps in the Coyol arc lavas between 12 and 7 Ma and 6 and 3.5 Ma. Our marine tephra layers cover the age range from 1 to 9 Ma and thus support the view of *Jordan et al.* [2007a, 2007b] of rather continuous Coyol magmatism and extend the activity at the Coyol arc to at least <2 Ma (Figures 7 and 8, and S3).

4.3.2.2. Las Sierras-Masaya Volcanic Complex
The Las Sierras Formation is a succession of mafic tephras, lahars, and lavas, including local phreatomagmatic tuffs and scoria deposits as well as widespread ignimbrites that may be related to formation of the Las Nubes caldera [*Girard and Van Wyk de Vries*, 2005]. The age of the Las Sierras-Masaya volcanic complex is uncertain; it may have started to form in the early Quaternary or even the Pliocene [*McBirney and Williams*, 1965] or just ~330 ka ago [*Carr et al.*, 2007b]. The youngest dated unit is a 34 ka old mafic ignimbrite at the west flank of the complex [*Kutterolf et al.*, 2007a]. A prominent product of a vent in the Las Nubes caldera is the 60 ka Fontana Tephra, a mafic Plinian fall deposit [*Williams*, 1983; *Wehrmann et al.*, 2006]. The younger Masaya caldera produced at least three large magmatic and phreatomagmatic eruptions between 6 and 1.8 ka prior to growth of the active Masaya volcano [*Bice*, 1985; *Kutterolf et al.*, 2007a; *Pérez and Freundt*, 2006; *Pérez et al.*, 2009].

The mafic tephras of the Las Sierras Formation have overlapping major-element glass compositions and very similar modal compositions (3–5% minerals; plagioclase > pyroxene > olivine [*Kutterolf et al.*, 2008a]), and the internal stratigraphy of the formation has yet to be established. Marine tephras therefore can only be compositionally related to the Las Sierras Formation in general. An exception is the correlation of marine tephra layer *D* from Sites U1381 and 1254 to the Fontana Tephra (FT), not only by glass composition (Figures 5a, 6a, 6b, 9, S1, and S2), but also by the outstanding high sideromelane/tachylite ratio and the age of ~56 ka estimated from sedimentation rates, which is very close to the age of ~60 ka that had been determined from sedimentation rates in gravity cores [*Kutterolf et al.*, 2008a].

The glass geochemistry of the Las Sierras Formation is found in widespread tephra layers *s3*, *s9*, *s10*, and *s15* (Figure 9; Sites 1254/55, 1039, 1040, 1242, U1381, and U1414), which cover the ~150 to ~750 ka age range, as well as in five individual marine ash beds of Sites U1381, U1378, and 1039 from ~60 to ~545 ka (Figures (7 and 8), and S3 and Table 3). These data show that the Las Sierras Formation dates much further back in time (>700 ka) than previously thought.

4.3.2.3. Malpaisillo Caldera

A thick pile of rhyolitic fallout deposits and ignimbrites surrounds the 10 km wide Malpaisillo Caldera, located ca. 50 km northwest of Managua (Figures 1 and 2). According to *Stoppa* [2015], this succession was emplaced between ~290 and ~610 ka, and comprises at least six major tephra units (Figure 2; LaPT = La Paz Centro Tephra, LaFT = La Fuente Tephra, ST = Sabanettas Tephra, TolT = Tolapa Tephra, LMN = Lower Maderas Negras Tephra, and UMT = Upper Maderas Negras Tephra). The individual tephras can be distinguished by their alkali contents (K_2O = 2.32–3.93 wt %; Na_2O = 3.6–5.3 wt %) and are all significantly more potassium-rich than other Pleistocene to Holocene Nicaraguan tephras. This allowed us to correlate tephra layers *G1* and *G2* in Sites 1039 and 1040 to the Malpaisillo caldera (Figures 5a, 6a, 6b, S1, and S2). The sedimentation-rate derived ages of the *G1* and *G2* layers are ~280 and ~380 ka, respectively, and they may relate to the large TolT and LaFT deposits.

4.3.3. Northern CAVA Provenance

The Early Pleistocene and older tephrostratigraphic successions of El Salvador and Guatemala are poorly known, but the Late Pleistocene through Holocene stratigraphy of major tephras is fairly well known [e.g., *Koch and McLean*, 1975; *Newhall*, 1981; *Petersen and Rose*, 1985; *Rose et al.*, 1987, 1999], and a geochemical data set for these major tephras is available [*Kutterolf et al.*, 2008a]. Thus, we are able to correlate one ash bed from Site U1378 (correlation *B1*) to the 36 ka old Terra Blanca 4 (TB4) tephra and one ash bed from Site 1040 (*B2*) to the older "A3/A5" tephras [*Kwasnitschka*, 2009], all from Ilopango Caldera in El Salvador (Figure 9). The marine tephra layer *E* (Figure 9; Sites 844, 1039, 1241, 1254, and 1255) correlates with the 84 ka Los Chocoyos tephra (LCY) [*Rose et al.*, 1999] from Atitlán Caldera (Figure S4). The LCY has been widely found in Pacific and Caribbean marine sediment cores [*Hahn et al.*, 1979; *Drexler et al.*, 1980; *Kutterolf et al.*, 2008a]. Tephra layer *F* (Figure 9; Sites 1242 and U1378) relates to the 191 ± 11 ka L-Fall Tephra (LFT) [*Rose et al.*, 1999], from the Amatilán Caldera in Guatemala (Figure S4). The LCY and LFT ashes found in our cores were emplaced ~800–1000 km away from their source volcano.

5. Conclusions

We have established a new and consistent tephrochronostratigraphy, which describes the occurrence of large explosive eruptions from southern CAVA volcanoes (Figure 9). Major widespread tephra layers, e.g., *D*, *G*, *H*, *O*, *P*, *T*, facilitate correlations between Nicaragua and Costa Rica, but also to northern CAVA tephra successions (e.g., *B*, *E*, and *F*; Guatemala and El Salvador). We have provided a stratigraphically classified tephra database of glass compositions of large-magnitude Quaternary and Neogene explosive eruptions. We have correlated marine tephra layers to their terrestrial counterparts, or along-arc provenance, and used the gathered information from previously dated terrestrial samples [e.g., *Alvarado and Gans*, 2012] and newly acquired Ar/Ar ages of marine tephra deposits to build an overall chronotephrostratigraphy for the southern CAVA. These data provide new insights into the overall lifetime and the number of major eruptions of the major volcanic complexes.

References

Abers, G. A., T. Plank, and B. R. Hacker (2003), The wet Nicaraguan slab, *Geophys. Res. Lett.*, 30, 1098, doi:10.1029/2002GL015649.
Alloway, B. V., G. Larsen, D. J. Lowe, P. A. R. Shane, and J. A. Westgate (2007), Tephrochronology, in *Encyclopaedia of Quaternary Science*, edited by S. A. Elias, pp. 2869–2898, Elsevier, London, U. K.
Alvarado, G. E., and M. J. Carr (1993), The Platanar-Aguas Zarcas volcanic centers, Costa Rica: Spatial-temporal association of Quaternary calc-alkaline and alkaline volcanism, *Bull. Volcanol.*, 55, 443–453.
Alvarado, G. E., and P. B. Gans (2012), Síntesis geocronológica del magmatismo, metamorfismo y metalogenia de Costa Rica, América Central, *Rev. Geol. Am. Cent.*, 46, 7–122.
Alvarado, G. E., S. Kussmaul, S. Chiesa, P.-Y. Gillot, H. Appel, G. Wörner, and C. Rundle (1992), Resumen chronoestratigráfico de las rocas ígneas de Costa Rica basado en dataciones radiométricas, *J. South Am. Earth Sci.*, 6(3), 151–168.
Alvarado, G. E., C. Dengo, U. Martens, J. Bundschuh, T. Aguilar, and S. Bonis (2007), Stratigraphy and geologic history, in *Central America: Geology, Resources, and Hazards*, edited by J. Bundschuh and G. E. Alvarado, pp. 345–394, Taylor and Francis, London, U. K.
Barckhausen, U., C. R. Ranero, R. von Huene, S. Cande, and H. Roeser (2001), Revised tectonic boundaries in the Cocos Plate off Costa Rica: Implications for the segmentation of the convergent margin and for plate tectonic models, *J. Geophys. Res.*, 106(19), 207–220.

Bice, D. C. (1985), Quaternary volcanic stratigraphy of Managua, Nicaragua: Correlation and source assignment for multiple overlapping plinian deposits, *Geol. Soc. Am. Bull.*, *96*(4), 553–566.

Bolge, L. L., M. J. Carr, K. I. Milidakis, F. N. Lindsay, and M. D. Feigenson (2009), Correlating geochemistry, tectonics, and volcanic volume along the Central American volcanic front, *Geochem. Geophys. Geosyst.*, *10*, Q12S18, doi:10.1029/2009GC002704.

Borgia, A., and B. Van Wyk de Vries (2003), The volcano-tectonic evolution of Concepcion, Nicaragua, *Bull. Volcanol.*, *65*, 248–266.

Bowles, F. A., R. N. Jack, and I. S. E. Carmichael (1973), Investigation of deep-sea volcanic ash layers from equatorial Pacific cores, *Geol. Soc. Am. Bull.*, *84*, 2371–2388.

Cai, Y., A. LaGatta, S. L. Goldstein, C. H. Langmuir, A. Gomez-Tuena, A. L. Martin del Pozzo, and G. Carrasco-Nunez (2014), Hafnium isotope evidence for slab melt contributions in hot slab arcs: An example of the Central Mexican Volcanic Belt, *Chem. Geol.*, *377*, 45–55, doi: 10.1016/j.chemgeo.2014.04.002.

Carey, S., and H. Sigurdsson (2000), Grain size of Miocene volcanic ash layers from Sites 998, 999, and 1000: Implications for source areas and dispersal, in *Proceedings Ocean Drilling Program Scientific Results*, vol. 165, edited by R. M. Leckie et al., pp. 101–110, Ocean Drill. Program, College Station, Tex.

Carey, S. N. (2000), Volcaniclastic sedimentation around island arcs, in *Encyclopedia of Volcanoes*, edited by H. Sigurdsson et al., pp. 627–642, Academic, New York.

Carr, M., M. D. Feigenson, L. C. Patino, and J. A. Walker (2003), Volcanism and geochemistry in Central America: Progress and problems, in *Inside the Subduction Factory, Geophys. Monogr.*, vol. 138, edited by J. Eiler, pp. 153–174, AGU, Washington, D. C.

Carr, M. J. (1984), Symmetrical and segmented variation of physical and geochemical characteristics of the Central American Volcanic Front, *J. Volcanol. Geotherm. Res.*, *20*, 231–252.

Carr, M. J., M. D. Feigensohn, and E. A. Benett (1990), Incompatible element and ipic evidence for tectonic control of source mixing and melt extraction along the central American arc, *Contrib. Mineral. Petrol.*, *105*, 369–380.

Carr, M. J., L. C. Patino, and M. D. Feigenson (2007a), Petrology and geochemistry of lavas, in *Central America—Geology, Resources and Hazards*, edited by J. Buntschuh and G. E. Alvarado, Balkema, Rotterdam, Netherlands.

Carr, M. J., I. Saginor, G. E. Alvarado, L. L. Bolge, F. N. Lindsay, K. Milidakis, B. D. Turrin, M. D. Feigensohn, and C. C. Swisher III (2007b), Element fluxes from the volcanic front of Nicaragua and Costa Rica, *Geochem. Geophys. Geosyst.*, *8*, Q06001, doi:10.1029/2006GC001396.

Chiesa, S. (1991), El Flujo de Pómez biotítica del Río Liberia (Guanacaste) Costa Rica, America Central, *Rev. Geol. Am. Cent.*, *13*, 73–84.

Chiesa, S., G. Civelli, P.-Y. Gillot, O. Mora, and G. E. Alvarado (1992), Rocas piroclásticas asociadas con La Formación de la Caldera de Guayabo, Cordillera de Guanacaste, Costa Rica, *Rev. Geol. Am. Cent.*, *14*, 59–75.

Clift, P. D., L. H. Chan, J. Blusztajn, G. D. Layne, M. Kastner, and R. K. Kelly (2005), Pulsed subduction accretion and tectonic erosion recon-structed since 2.5 Ma from the tephra record offshore Costa Rica, *Geochem. Geophys. Geosyst.*, *6*, Q09016, doi:10.1029/2005gc000963.

Dalrymple, G. B., E. C. Alexander Jr., M. A. Lanphere, and G. P. Kraker (1981), Irradiation of samples for ⁴⁰Ar/³⁹Ar dating using the Geological Survey TRIGA reactor, *U.S. Geol. Surv. Prof. Pap.*, *1176*, 55 pp.

Deering, C. D., T. A. Vogel, L. C. Patino, and G. E. Alvarado (2007), Origin of distinct silicic magma types from the Guachipelín Caldera, NW Costa Rica: Evidence for magma mixing and protracted subvolcanic residence, *J. Volcanol. Geotherm. Res.*, *165*(3), 103–126.

Defant, M. J., T. E. Jackson, M. S. Drummond, J. Z. de Boer, M. D. Feigenson, R. C. Maury, and R. H. Stewart (1992), The geochemistry of young volcanism throughout western Panama and southeastern Costa Rica: An overview, *J. Geol. Soc. London*, *149*, 569–579.

DeMets, C. (2001), A new estimate for present-day Cocos-Caribbean plate motion: Implications for slip along the Central American volcanic arc, *Geophys. Res. Lett.*, *28*, 4043–4046.

Drexler, J. W., W. I. Rose Jr., R. S. J. Sparks, and M. T. Ledbetter (1980), The Los Chocoyos Ash, Guatemala: A major stratigraphic marker in Middle America and in the three ocean basins, *Quat. Res.*, *13*, 327–345.

Ehrenborg, J. (1996), A new stratigraphy for the Tertiary volcanic rocks of the Nicaraguan highland, *Geol. Soc. Am. Bull.*, *108*, 830–842.

Feigenson, M. D., and M. J. Carr (1986), Positively correlated Nd and Sr isotope ratios of lavas from the Central American volcanic front, *Geology*, *14*, 79–82.

Feigenson, M. D., M. J. Carr, S. V. Maharaj, L. L. Bolge, and S. Juliano (2004), Lead isotope composition of Central American Volcanoes: Influ-ence of the Galápagos Plume, *Geochem. Geophys. Geosyst.*, *5*, Q06001, doi:10.1029/2003GC000621.

Fietzke, J., V. Liebetrau, D. Günther, K. Gürs, K. Hametner, K. Zumholz, T. H. Hansteen, and A. Eisenhauer (2008), An alternative data acquisi-tion and evaluation strategy for improved isotope ratio precision using LA-MC-ICP-MS applied to stable and radiogenic strontium iso-topes in carbonates, *J. Anal. At. Spectrom.*, *23*(7), 955–961.

Freundt, A., S. Kutterolf, H. U. Schmincke, T. H. Hansteen, H. Wehrmann, W. Pérez, W. Strauch, and M. Navarro (2006), Volcanic hazards in Nicaragua: Past, present, and future, *Spec. Pap. Geol. Soc. Am.*, *412*, 141–165.

Freundt, A., R. Halama, E. Suess, and D. Völker (2014), Introduction to the special issue on SFB 574 ''Volatiles and fluids in subduction zones: Climate feedback and trigger mechanisms for natural disasters,'' *Int. J. Earth Sci.*, *103*(7), 1729–1731, doi:10.1007/s00531-014-1059-9.

Freundt, A., A. Hartmann, S. Kutterolf, and W. Strauch (2010), Volcaniclastic stratigraphy of the Tiscapa maar crater walls (Managua, Nicara-gua): Implications for volcanic and seismic hazards and Holocene climate changes, *Int. J. Earth. Sci.*, *99*, 1453–1470, doi:10.1007/s00531-009-0469-6.

Funk, J., P. Mann, K. McIntosh, and J. Stephens (2009), Cenozoic tectonics of the Nicaraguan depression, Nicaragua, and Median Trough, El Salvador, based on seismic reflection profiling and remote-sensing data, *Geol. Soc. Am. Bull.*, *121*, 1491–1521.

Gazel, E., and P. Ruiz (2005), Los conos piroclásticos de Sabana Redonda: Componente magmático enriquecido del volcán Poás, Costa Rica, *Rev. Geol. Am. Cent.*, *33*, 45–60, doi:10.15517/rgac.v0i33.4235.

Gazel, E., M. Carr, K. Hoernle, M. D. Feigenson, D. Szymanski, F. Hauff, and P. van den Bogard (2009), Galápagos-OIB signature in southern Central America: Mantle refertilization by arc–hotspot interaction, *Geochem. Geophys. Geosyst.*, *10*, Q02S11, doi:10.1029/2008GC002246.

Gillot, P. Y., S. Chiesa, and G. Alvarado (1994), Chronostratigraphy and evolution of the Neogene–Quaternary volcanism in north Costa Rica: The Arenal volcano-structural frame work, *Rev. Geol. Am. Cent.*, *17*, 45–53.

Girard, G., and B. van Wyk de Vries (2005), The Managua Graben and Las Sierras-Masaya volcanic complex (Nicaragua); pull-apart localiza-tion by an intrusive complex: Results from analogue modeling, *J. Volcanol. Geotherm. Res.*, *144*, 37–57.

Günther, D., S. E. Jackson, and H. P. Longerich (1999), Laser ablation and arc/spark solid sample introduction into inductively coupled plas-ma mass spectrometers, *Spectrochim. Acta B*, *54*(3), 381–409.

Hahn, G. A., W. I. Rose, and T. Meyers (1979), Geochemical correlation of genetically related rhyolitic ash-flow and air-fall ashes, central and western Guatemala and the equatorial Pacific, *Spec. Pap. Geol. Soc. Am.*, *180*, 101–112.

Hannah, R. S., T. A. Vogel, L. C. Patino, G. E. Alvarado, W. Peréz, and D. R. Smith (2002), Origin of silicic volcanic rocks in Central Costa Rica: A study of a chemically variable ash-flow sheet in the Tiribí Tuff, *Bull. Volcanol.*, *64*, 117–133.

Harris, R. N., A. Sakaguchi, K. Petronotis, and the Expedition 344 Scientists (2013), *Proceedings of Integrated Ocean Drilling Program*, vol. 344, Integrated Ocean Drill. Program, College Station, Tex., doi:10.2204/iodp.proc.344.2013.

Hoernle, K., R. Werner, J. P. Morgan, D. Garbe-Schoenberg, J. Bryce, and J. Mrazek (2000), Existence of complex spatial zonation in the Galápagos plume for at least 14 m.y., *Geology*, *28*(5), 435–438.

Hoernle, K., P. van den Bogaard, R. Werner, B. Lissinna, G. E. Alvarado, and C.-D. Garbe-Schönberg (2002), Missing history (16-71 Ma) of the Galápagos hotspot: Implications for the tectonic and biological evolution of the Americas, *Geology*, *30*(9), 795–798.

Hoernle, K., et al. (2008), Arc-parallel flow in the mantle wedge beneath Costa Rica and Nicaragua, *Nature*, *451*, 1094–1097.

Huey, P. E. (2009), IODP drilling and coring technology—Past and present, *Final Rep. PN119160*, 18 pp., Stress Eng. Serv. Inc., Houston, Tex. [Available at http://www.iodp.org/doc_download/3464-iodp-drilling-coring-tech-final.]

Hunt, J. B., and P. G. Hill (2001), Tephrological implications of beam size—Sample-size effects in electron microprobe analysis of glass shards, *J. Quat. Sci.*, *16*(2), 105–117.

Jordan, B. R., H. Sigudsson, S. N. Carey, R. Rogers, and J. Ehrenborg (2006), Geochemical correlation of Caribbean Sea tephra layers with ignimbrites in Central America, in *Neogene-Quaternary Continental Margin Volcanism: A Perspective From México*, vol. 402, edited by C. Siebe, J. L. Macías, and G. J. Aguirre-Díaz, pp. 175–208, doi:10.1130/2006.2402(08).

Jordan, B. R., H. Sigudsson, S. N. Carey, S. Lundin, R. Rogers, B. Singer, and M. Barguero-Molina (2007a), Petrogenesis of Central American Tertiary ignimbrites and associated Caribbean Sea tephra, *Spec. Pap. Geol. Soc. Am.*, *295*, 115–179.

Jordan, B. R., H. Sigurdsson, S. N. Carey, R. Rogers, and J. Ehrenborg (2007b), Geochemical variation along and across the Central American Miocene paleoarc in Honduras and Nicaragua, *Geochim. Cosmochim. Acta*, *71*, 3581–3591.

Keller, J., W. B. F. Ryan, D. Ninkovich, and R. Altherr (1978), Explosive volcanic activity in the Mediterranian over the past 200.000 years as recorded in deep-sea sediments, *Geol. Soc. Am. Bull.*, *89*, 591–604.

Kimura, G., et al. (1997), *Proceedings of Ocean Drilling Program Initial Reports*, vol. 170, 458 pp., Ocean Drill. Program, College Station, Tex.

Koch, A. J., and H. McLean (1975), Pleistocene tephra and ash-flow deposits in the volcanic highlands of Guatemala, *Geol. Soc. Am. Bull.*, *86*, 529–541.

Kuiper, K. F., A. Deino, F. J. Hilgen, W. Krijgsman, P. R. Renne, and J. R. Wijbrans (2008), Synchronizing rock clocks of Earth history, *Science*, *320*, 500–504, doi:10.1126/science.1154339.

Kutterolf, S., A. Freundt, W. Pérez, H. Wehrmann, and H.-U. Schmincke (2007a), Late Pleistocene to Holocene temporal succession and magnitudes of highly-explosive volcanic eruptions in west-central Nicaragua, *J. Volcanol. Geotherm. Res.*, *163*, 55–82.

Kutterolf, S., U. Schacht, H. Wehrmann, A. Freundt, and T. Mörz (2007b), Onshore to offshore tephrostratigraphy and marine ash layer diagenis in Central America, in *Central America—Geology, Resources and Hazards*, edited by J. Buntschuh and G. E. Alvarado, pp. 395–423, Taylor and Francis, Lisse, Netherlands.

Kutterolf, S., A. Freundt, W. Pérez, T. Mörz, U. Schacht, H. Wehrmann, and H.-U. Schmincke (2008a), The Pacific offshore record of Plinian arc volcanism in Central America: 1. Along-arc correlations, *Geochem. Geophys. Geosyst.*, *9*, Q02S01, doi:10.1029/2007GC001631.

Kutterolf, S., A. Freundt, and W. Pérez (2008b), The Pacific offshore record of Plinian arc volcanism in Central America: 2. Tephra volumes and erupted masses, *Geochem. Geophys. Geosyst.*, *9*, Q02S02, doi:10.1029/2007GC001791.

Kutterolf, S., A. Freundt, U. Schacht, D. Bürk, R. Harders, T. Mörz, and W. Pérez (2008c), The Pacific offshore record of Plinian arc volcanism in Central America: 3. Application to forearc geology, *Geochem. Geophys. Geosyst.*, *9*, Q02S03, doi:10.1029/2007GC001826.

Kutterolf, S., V. Liebetrau, T. Mörz, A. Freundt, T. Hammerich, and D. Garbe-Schönberg (2008d), Lifetime and cyclicity of fluid venting at fore-arc mound structures determined by tephrostratigraphy and radiometric dating of authigenic carbonates, *Geology*, *36*(9), 707–710, doi:10.1130/G24806A.1.

Kutterolf, S., A. Freundt, and C. Burkert (2011), Eruptive history and magmatic evolution of the 1.9 kyr Plinian dacitic Chiltepe Tephra from Apoyeque volcano in west-central Nicaragua, *Bull. Volcanol.*, *73*(7), 811–831.

Kutterolf, S., M. Jegen, J. X. Mitrovica, T. Kwasnitschka, A. Freundt, and P. Huybers (2013), A detection of Milankovitch frequencies in global volcanic activity, *Geology*, *41*(2), 227–230.

Kutterolf, S., et al. (2014), Large volume submarine ignimbrites in the Shikoku Basin: An example for explosive volcanism in the Western Pacific during the Late Miocene, *Geochem. Geophys. Geosyst.*, *15*, 1837–1851, doi:10.1002/2014GC005263.

Kutterolf, S., T. H. Hansteen, A. Freundt, H. Wehrmann, K. Appel, K. Krüger, and W. Peréz (2015), Bromine and chlorine emissions from Plinian eruptions along the Central American Volcanic Arc: From source to atmosphere, *Earth Planet. Sci. Lett.*, *429*, 234–246, doi:10.1016/j.epsl.2015.07.064.

Kutterolf, S., et al. (2016), A 400-ka tephrochronological framework for Central America from Lake Petén Itzá (Guatemala) sediments, *Quat. Sci. Rev.*, *150*, 200–220.

Kwasnitschka, T. (2009), Volcanic and tectonic development of the Ilopango Caldera, El Salvador: Stratigraphic correlation and visualization of emplacement, diploma thesis, 218 pp., Univ. of Kiel, Kiel, Germany.

Ledbetter, M. T. (1985), Tephrochronology of marine tephra adjacent to Central America, *Geol. Soc. Am. Bull.*, *96*, 77–82.

Le Maitre, R. W., et al. (2002), *Igneous Rocks: A Classification and Glossary of Terms: Recommendations of the International Union of Geological Sciences Subcommission of the Systematics of Igneous Rocks*, Cambridge Univ. Press, Cambridge, U. K.

Longpré, M. A., J. Stix, C. Burkert, T. Hansteen, and S. Kutterolf (2014), Sulfur budget and global climate impact of the AD 1835 eruption of Cosigüina volcano, Nicaragua, *Geophys. Res. Lett.*, *41*, 6667–6675, doi:10.1002/2014GL061205.

Maas, R., M. B. Kamenetsky, A. V. Sobolev, V. S. Kamenetsky, and N. V. Sobolev (2005), Sr-Nd-Pb isotopic evidence for a mantle origin of alkali chlorides and carbonates in the Udachnaya kimberlite, Siberia, *Geology*, 35, 549–552.

Machida, H. (1999), The stratigraphy, chronology and distribution of distal marker-tephras in and around Japan, *Global Planet. Change*, *21*, 71–94.

Martinez, M., and J. G. Viramonte (1971), *Geologia de la Cordillera Marrabios*, Catastro e Inventario de Recursos Naturales, Managua.

McBirney, A. R., and H. Williams (1965), *Volcanic History of Nicaragua*, vol. 55, pp. 1–65, Univ. of Calif. Press, Berkeley.

Mix, A. C., et al. (2003), *Proceeding of Ocean Drilling Program Initial Reports*, vol. 202, Ocean Drill. Program, College Station, Tex., doi:10.2973/odp.proc.ir.202.2003.

Molina, F., J. Martí, G. Aguirre, E. Vega, and L. Chavarría (2014), Stratigraphy and structure of the Cañas Dulces caldera (Costa Rica), *Geol. Soc. Am. Bull.*, *126*(11–12), 1465–1480.

Morris, J. D., et al. (2003), *Proceedings of Ocean Drilling Program Initial Reports*, vol. 205, Ocean Drill. Program, College Station, Tex., doi:10.2973/odp.proc.ir.205.2003.

Münker, C., S. Weyer, E. Scherer, and K. Mezger (2001), Separation of high field strength elements (Nb, Ta, Zr, Hf) and Lu from rock samples for MC-ICPMS measurements, *Geochem. Geophys. Geosyst.*, *2*(12), 1064, doi:10.1029/2001GC000183.

Newhall, C. G. (1981), Geology of the Lake Atitlan area, Guatemala: A study of subduction zone volcanism and caldera formation, PhD thesis, 364 pp., Dartmouth Coll., Hanover, N. H.

Norman, M. D., N. J. Pearson, A. Sharma, and W. L. Griffin (1996), Quantitative analysis of trace elements in geological materials by laser ablation ICPMS: Instrumental operating conditions and calibration values of NIST glasses, *Geostand. Newsl.*, *20*, 247–261.

Nowell, G. M., P. D. Kempton, S. R. Noble, J. G. Fitton, A. D. Saunders, J. J. Mahoney, and R. N. Taylor (1998), High precision Hf isotope measurements of MORB and OIB by thermal ionisation mass spectrometry: Insights into the depleted mantle, *Chem. Geol.*, *149*(3–4), 211–233.

Patino, L. C., M. Carr, and M. D. Feigenson (1997), Cross-arc geochemical variations in volcanic fields in Honduras C.A.: Progressive changes in source with distance from the volcanic front, *Contrib. Mineral. Petrol.*, *129*, 341–351.

Patino, L. C., M. Carr, and M. D. Feigenson (2000), Local and regional variations in Central American arc lavas controlled by variations in subducted sediment input, *Contrib. Mineral. Petrol.*, *138*, 256–283.

Pérez, W., and A. Freundt (2006), The youngest highly explosive basaltic eruptions from Masaya Caldera Complex (Nicaragua): Stratigraphy and hazard assessment, *Spec. Pap. Geol. Soc. Am.*, *412*, 189–207, doi:10.1130/2006.2412(10).

Pérez, W., G. E. Alvarado, and P. B. Gans (2006), The 322 ka Tiribí Tuff: Stratigraphy, geochronology and mechanisms of deposition of the largest and most recent ignimbrite in the Valle Central, Costa Rica, *Bull. Volcanol.*, *69*, 25–40.

Pérez, W., A. Freundt, S. Kutterolf, and H.-U. Schmincke (2009), The Masaya Triple Layer: A 2100 year old basaltic multi-episodic Plinian eruption from the Masaya Caldera Complex (Nicaragua), *J. Volcanol. Geotherm. Res.*, *179*, 191–205.

Petersen, P. S., and W. I. Rose (1985), Explosive eruptions of the Ayarza calderas, southeastern Guatemala, *J. Volcanol. Geotherm. Res.*, *25*, 289–307.

Pin, C., D. Briot, C. Bassin, and F. Poitrasson (1994), Concomitant separation of strontium and samarium-neodymium for isotopic analysis in silicate samples, based on specific extraction chromatography, *Anal. Chim. Acta*, *298*, 209–217.

Pin, C., and J. F. Santos-Zalduegui (1997), Sequential separation of light rare-earth elements, thorium and uranium by miniaturized extraction chromatography: Application to isotopic analyses of silicate rocks, *Anal. Chim. Acta*, *339*, 79–89.

Pisias, N. G., L. A. Mayer, T. R. Janecek, A. Palmer-Julson, and T. H. von Andel (Eds.) (1995), *Proceedings of Ocean Drilling Program Scientific Results*, vol. 138, Ocean Drill. Program, College Station, Tex.

Plank, T., V. Balzer, and M. Carr (2002), Nicaraguan volcanoes record paleoceanographic changes accompanying closure of the Panama gateway, *Geology*, *30*, 1087–1090.

Ponomareva, V., M. Portnyagin, A. Derkachev, I. F. Pendea, J. Bourgeois, P. J. Reimer, D. Garbe-Schönberg, S. Krasheninnikov, and D. Nürnberg (2013), Early Holocene M 6 explosive eruption from Plosky volcanic massif (Kamchatka) and its tephra as a link between terrestrial and marine paleoenvironmental records, *Int. J. Earth Sci.*, *102*(6), 1673–1699.

Prosser, J. T., and M. J. Carr (1987), Poás volcano, Costa Rica: Geology of the summit region and spatial and temporal variations among the most recent lavas, *J. Volcanol. Geotherm. Res.*, *33*(1), 131–146.

Rose, W. I., C. G. Newhall, T. J. Bornhorst, and S. Self (1987), Quaternary silicic pyroclastic deposits of Atitlàn Caldera, Guatemala, *J. Volcanol. Geotherm. Res.*, *33*, 57–80.

Rose, W. I., F. M. Conway, C. R. Pullinger, A. Deino, and K. McIntosh (1999), An improved age framework for late Quaternary silicic eruptions in northern Central America, *Bull. Volcanol.*, *61*, 106–120.

Ruiz, P., E. Gazel, G. E. Alvarado, M. Carr, and G. J. Soto (2010), Caracterización geoquímica y petrográfica de las unidades geológicas del macizo del volcán Poás, Costa Rica, *Rev. Geol. Am. Cent.*, *43*, 37–66.

Ryan, W. B. F., et al. (2009), Global multi-resolution topography synthesis, *Geochem. Geophys. Geosyst.*, *10*, Q03014, doi:10.1029/2008GC002332.

Sáenz, R. (1982), Edades radiométricas de algunas rocas de Costa Rica, *Bol. Vulcanol.*, *12*, 8–10.

Saginor, I., E. Gazel, M. J. Carr, C. C. Swisher III, and B. Turrin (2011a), Progress and challenges using 40Ar/39Ar geochronology in Costa Rica and Nicaragua, *Rev. Geol. Am. Cent.*, *45*, 75–85.

Saginor, I., E. Gazel, M. J. Carr, C. C. Swisher III, and B. Turrin (2011b), New Pliocene, Pleistocene 40Ar/39Ar ages fill in temporal gaps in the Nicaraguan volcanic record, *J. Volcanol. Geotherm. Res.*, *202*(1), 143–152.

Schindlbeck, J. C., S. Kutterolf, A. Freundt, S. M. Straub, K.-L. Wang, M. Jegen, S. R. Hemming, A. T. Baxter, and M. I. Sandoval (2015), The Miocene Galápagos ash layer record of Integrated Ocean Drilling Program Legs 334 and 344: Ocean-island explosive volcanism during plume-ridge interaction, *Geology*, *43*(7), 599–602.

Schindlbeck, J. C., S. Kutterolf, A. Freundt, G. D. M. Andrews, K.-L. Wang, D. Völker, R. Werner, M. Frische, and K. Hoernle (2016a), Alkalic marine tephra layers at ODP Site 1241-major explosive eruptions from an oceanic volcano in a pre-shield stage?, *J. Volcanol. Geotherm. Res.*, doi:10.1016/j.jvolgeores.2016.10.009, in press.

Schindlbeck, J. C., S. Kutterolf, A. Freundt, S. M. Straub, P. Vannucchi, and G. E. Alvarado (2016b), Late Cenozoic tephrostratigraphy offshore the southern Central American Volcanic Arc: 2. Implications for magma production rates and subduction erosion, *Geochem. Geophys. Geosyst.*, doi:10.1002/2016GC006504, in press.

Scott, W., C. Gardner, G. Devoli, and A. Alvarez (2006), The AD 1835 eruption of Volcán Cosigüina, Nicaragua: A guide for assessing local volcanic hazards, *Spec. Pap. Geol. Soc. Am.*, *412*, 167–187.

Self, S., M. R. Rampino, and M. Carr (1989), A reappraisal of the 1835 eruption of Coseguina and its atmospheric impact, *Bull. Volcanol.*, *52*, 57–65.

Semm, W., and G. E. Alvarado (2007), Ignimbrites of the Pliocene Bagaces Formation near Cañas (Guanacaste, Costa Rica), *Neues Jahrbuch für Geologie und Paläontologie - Abhandlungen*, *246*(3), 313–323.

Soto, G. J., and G. E. Alvarado (2006), Eruptive history of Arenal Volcano, Costa Rica, 7ka to present, *J. Volcanol. Geotherm. Res.*, *157*, 254–269.

Soto, G. J., G. E. Alvarado, and S. Goold (2003), Erupciones <3800 a.P. del volcán Rincón de La Vieja, Costa Rica, *Rev. Geol. Am. Cent.*, *29*, 67–86.

Stoppa, L. (2015), Tephrachronostratigraphy of the Malpaisillo Caldera (Central-western Nicaragua), MS thesis, 155 pp., Univ. de Fribourg, Fribourg, Switzerland.

Sussman, D. (1985), Apoyo Caldera, Nicaragua: A major Quaternary silicic eruptive center, *J. Volcanol. Geotherm. Res.*, *24*, 249–282.

Syracuse, E. M., and G. A. Abers (2006), Global compilation of variations in slab depth beneath arc volcanoes and implications, *Geochem. Geophys. Geosyst.*, *7*, Q05017, doi:10.1029/2005GC001045.

Szymanski, D., L. Patino, T. Vogel, and G. Alvarado (2013), Evaluating complex magma mixing via polytopic vector analysis (PVA) in the Papagayo Tuff, Northern Costa Rica: Processes that form continental crust, *Geosciences*, *3*(3), 585.

Todt, W., R. A. Cliff, A. Hanser, and A. W. Hofmann (1996), Evaluation of a [202]Pb-[205]Pb double-spike for high-precision lead isotope analysis, in *Earth Processes: Reading the Isotopic Code*, edited by A. Basu and S. R. Hart, pp. 429–437, AGU, Washington, D. C.

Tournon, J., and G. Alvarado (1997), Mapa geológica de Costa Rica, incluyendo Folleto explicativo, Instituto Tecnológico de Costa Rica, Costa Rica, 79 pp., y Mapa 1:500000.

van Achterberg, E., C. G. Ryan, S. E. Jackson, and W. Griffin (2001), LA-ICP-MS in the Earth Sciences—Appendix 3, data reduction software for LA-ICP-MS, in *Short Course*, vol. 29, edited by P. J. Sylvester, pp. 239–243, Mineral. Assoc. of Can., St. John's, Newfoundland and Labrador, Canada.

Vannucchi, P., K. Ujiie, N. Stroncik, and the Expedition 334 Scientists (2012), *Proceedings of Integrated Ocean Drilling Program*, vol. 334, Integrated Ocean Drill. Program Manage. Int., Inc., Tokyo.

Villegas, A. (2004), La formación Alto Palomo: flujos pumíticos de la cordillera volcanica Central, Costa Rica, *Rev. Geol. Am. Cent.*, *30*, 73–81.

Vogel, T. A., L. C. Patino, G. E. Alvarado, and P. B. Gans (2004), Silicic ignimbrites within the Costa Rican volcanic front: Evidence for the formation of continental crust, *Earth Planet. Sci. Lett.*, *226*, 149–159.

Vogel, T., L. Patino, G. E. Alvarado, and W. I. Rose (2007), Petrogenesis of ignimbrites, in *Central America—Geology, Resources and Hazards*, vol. 1, edited by J. Bundschuh and G. E. Alvarado, pp. 591–619, Balkema, Tokyo.

Walker, J. A., J. E. Mickelson, R. B. Thomas, L. C. Patino, B. Cameron, M. J. Carr, M. D. Feigenson, and R. L. Edwards (2007), U-series disequilibria in Guatemalan lavas, crustal contamination, and implications for magma genesis along the Central American subduction zone, *J. Geophys. Res.*, *112*, B06205, doi:10.1029/2006JB004589.

Walker, J. D., J. W. Geissman, S. Bowring, and L. Babcock (2013), The Geological Society of America geologic time scale, *Geol. Soc. Am. Bull.*, *125*(3–4), 259–272.

Wark, D. A. (1991), Oligocene ash flow volcanism, Northern Sierra Madre Occidental: Role of mafic and intermediate-composition magmas in rhyolite genesis, *J. Geophys. Res.*, *96*, 389–411.

Wehrmann, H., C. Bonadonna, A. Freundt, B. F. Houghton, and S. Kutterolf (2006), Fontana Tephra: A basaltic plinian eruption in Nicaragua, *Spec. Pap. Geol. Soc. Am.*, *412*, 209–223.

Weyl, R. (1980), Geology of Central America, in *Beiträge zur regionalen Geologie der Erde*, vol. 15, edited by F. E. A. Bender, 2nd ed., 371 pp., Gebr. Borntraeger, Berlin.

Williams, S. N. (1983), Geology and eruptive mechanisms of Masaya Caldera Complex, Nicaragua, PhD thesis, 169 pp., Dartmouth Coll., Hanover, N. H.

Wise, S. A. and R. L. Watters (2012), National Institute of Standards and Technology Website. [Available at http://www.nist.gov/srm.]

Woodhead, J. D., and J. M. Hergt (2001), Strontium, neodymium and lead isotope analyses of NIST glass certified reference materials: SRM 610, 612, 614, *Geostand. Geoanal. Res.*, *25*, 261–226.

Zamora, N., J. Méndez, M. Barahona, and L. Sjöbohm (2004), Volcano-estratigrafía asociada al campo de domos de Cañas Dulces, Guanacaste, Costa Rica, *Rev. Geol. Am. Cent.*, *30*, 41–58.